# Enzyme Encapsulation in a Porous Hydrogen-Bonded Organic Framework

Weibin Liang[†▽], Francesco Carraro[§▽], Marcello B. Solomon[§], Stephen G. Bell[†], Heinz Amenitsch[‖], Christopher J. Sumby*[†], Nicholas G. White*[‡], Paolo Falcaro*[§,†], Christian J. Doonan*[†]

[†] Department of Chemistry and the Centre for Advanced Nanomaterials, The University of Adelaide, Adelaide, South Australia 5005, Australia

[§] Institute of Physical and Theoretical Chemistry, Graz University of Technology, Stremayrgasse 9, Graz 8010, Austria

[‖] Institute of Inorganic Chemistry, Graz University of Technology, Stremayrgasse 9, Graz 8010, Austria

[‡] Research School of Chemistry, The Australian National University, Canberra, ACT, Australia

[▽] These authors contribute equally to the article

**ABSTRACT:** Protection of biological assemblies is critical to applications in biotechnology, increasing the durability of enzymes in biocatalysis or potentially stabilizing biotherapeutics during transport and use. Here we show that a porous hydrogen-bonded organic framework (HOF) constructed from water soluble tetra-amidinium (**1**·$Cl_4$) and tetracarboxylic acid ($H_4$**2**) building blocks can encapsulate and stabilize biomolecules to elevated temperature, proteolytic and denaturing agents, and extend the operable pH range for catalase activity. The HOF, which readily retains water within its framework structure, can also protect and retain the activity of enzymes such as alcohol oxidase, that are inactive when encapsulated within zeolitic imidazolate framework (ZIF) materials. Such HOF coatings could provide valid alternative materials to ZIFs: they are metal free, possess larger pore apertures, and are stable over a wider, more biologically relevant pH range.

## INTRODUCTION

Protection of biological assemblies is critical to applications in biotechnology, such as biocatalysis and therapeutics, which often expose enzymes to harsh environments known to have deleterious effects on their native activity.[1, 2] One approach to enhance enzyme stability is to immobilize them within porous materials. Indeed, research has shown that post-infiltration of enzymes into mesoporous silicas,[3] metal-organic frameworks (MOFs)[4], and covalent-organic frameworks[5] offers a level of protection from organic solvents and elevated temperatures. However, infiltration of guests into pre-synthesized materials has the inherent limitation that the pore apertures of the host material are larger than the diameter of the guest protein molecule. Recently, we and others have reported a different approach where biomolecules and assemblies thereof (e.g. enzymes[6-11] and viruses[12-14]) induce the growth of MOFs to form a porous coating that significantly increases their durability when exposed to challenging conditions. In this process, the MOF components self-assemble around the biomolecule encapsulating it within its porous crystalline matrix. This facile encapsulation method is carried out in aqueous solution at room temperature to ensure minimal disruption to the structure of the biomolecule. As a result, the strategy is limited to MOFs that are compatible with these synthetic requirements. Zeolitic imidazolate framework-8 (ZIF-8), and related ZIF materials, have been proven to be excellent candidates for the synthesis of bio-composites.[15-18]

Although ZIFs possess many properties that make them favorable for studying biomolecule encapsulation, they present challenges for certain applications. For example, the structure topologies observed for reported ZIF biocomposites possess narrow crystallographic pore apertures (typically ~ 3.4 Å) that significantly limit the size of substrates that can be used for biocatalytic transformations.[19, 20] In addition, ZIF-8 can decompose in the presence of certain buffer solutions,[21, 22] chelating agents,[14] and at mildly acidic pH.[23, 24] This instability can limit the diversity of chemistry that can be explored for such systems. Thus, to develop this area of porous framework chemistry we sought to uncover new materials for the encapsulation and protection of biomolecules.

Another class of crystalline materials that may be synthesized via a building block approach are hydrogen-bonded organic frameworks (HOFs).[24-28] HOFs are porous network materials assembled by hydrogen bonding between organic components, and are often highly crystalline and can be prepared in mild conditions. Prototypical systems were first prepared in the 1990s,[29, 30] while more recent examples have been shown to be surprisingly stable

and/or permanently porous.[25, 31, 32] While HOFs are often incompatible with polar organic solvents such as DMF and DMSO,[27] we have recently reported frameworks prepared from poly-amidinium and poly-carboxylate tectons, which are stable in water and polar solvents, even at 100 °C.[33, 34] Given these properties, we hypothesized that such HOFs could encapsulate biomolecules to form a new class of porous, crystalline biocomposites. HOFs share analogous synthetic design principles with MOFs[35, 36] which offers opportunities to construct composites of bespoke pore shape, size and functionality. However, they have the advantage of being metal free which is desirable for some biological applications.[37, 38]

Here we report the synthesis, characterization and catalytic activity of HOF-based biocomposites synthesized from tetra-amidinium (**1**·$Cl_4$) and tetracarboxylic acid ($H_4$**2**) building blocks (Figure 1 and S1). Throughout this work we refer to this biocompatible HOF as BioHOF-1, and enzymes encapsulated with this HOF as enzyme@BioHOF-1. These crystalline composites are stable in water over a wide pH range (5-10), polar organic solvents and phosphate buffers. Further, they possess pore dimensions (limiting pore diameter *ca.* 6.4 Å) that significantly exceed those found ZIF-based materials of sodalite topology (*ca.* 3.4 Å). We show that the HOF coating protects encapsulated enzymes (FITC-tagged catalase, FCAT, and FITC-tagged alcohol oxidase, FAOx) from elevated temperatures, a proteolytic enzyme (trypsin) and a chaotropic agent (urea). Also, in the case of FCAT, the HOF coating extends its maximum activity over a broad pH range (5 to 10). Interestingly, FAOx retains enzymatic activity within the HOF; however, the same enzyme shows no activity when adsorbed on, or encapsulated in ZIF materials. This provides a clear example of how HOFs can expand the chemistry of enzyme encapsulation in crystalline frameworks. We believe that the control over the topology, pore structure, and chemistry offered by HOFs will provide new opportunities to capitalize on bioactive composites for applications in bio-catalysis and bio-medicine.

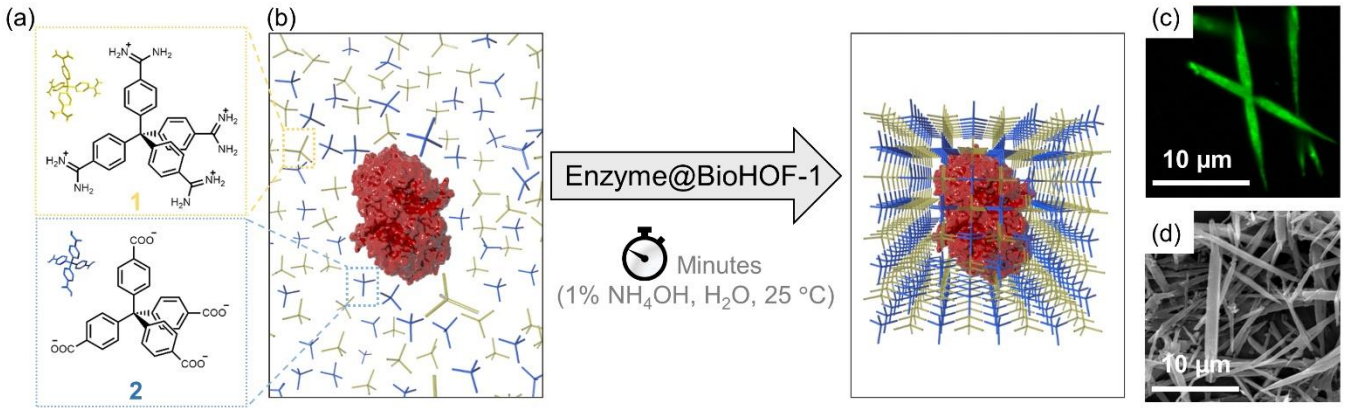


**Figure 1**. (a) Chemical structures of the BioHOF-1 components. (b) A schematic representation of the synthesis of enzyme@BioHOF-1 composites. (c) CLSM images of the as-synthesized FCAT@BioHOF-1 composite and (d) SEM image of FCAT@BioHOF-1 crystals. SEM images of BioHOF-1, FCAT@BioHOF-1, and FAOx@BioHOF-1 are reported in Figure S8.

## RESULTS AND DISCUSSION

Recently, some of us reported that amidinium and carboxylate functionalized organic molecules could assemble in aqueous solutions to rapidly form porous crystalline networks via charge-assisted hydrogen bonds.[33, 34] The biocompatible synthesis and stability towards a range of common organic solvents (polar and non-polar) led us to hypothesize that these novel HOFs could form biocomposites analogous to those reported for ZIFs. Accordingly, we selected **1** and **2** (Figure 1 and S1) as building units as they are known to form an open framework structure (Figure S2), here termed BioHOF-1, with limiting pore dimensions of *ca.* 6.4 Å (Figure S1). Initial studies targeted the encapsulation of catalase (CAT), a tetrameric enzyme (9.7 × 9.2 × 6.7 nm) that catalyzes the splitting of hydrogen peroxide to water and oxygen[39] (fluorescein-tagged catalase, FCAT, was used herein to facilitate microscopy analysis). Our previous work on ZIF-8 suggested that biocomposite synthesis was facilitated *via* the accumulation of $Zn^{2+}$ cations at the protein surface.[40] With this in mind we employed dynamic light scattering (DLS) to measure the difference in hydrodynamic diameter ($D_h$) of FCAT after addition of the amidinium and carboxylate functionalized building blocks, respectively. Addition of the positively charged amidinium link to a solution containing FCAT (measured zeta potential -15.8 ± 0.1 mV) engendered an increase in $D_h$ from 10.8 ± 1.0 to 2050 ± 578.4 nm (Table S1). However, adding the carboxylate-functionalized link did not change the $D_h$ of FCAT (Table S1). These data support the hypothesis that electrostatic attraction between the protein surface and framework components are important in promoting the initial formation of the HOF biocomposites. To this end, FCAT@BioHOF-1 composites were synthesized by adding positively charged **1** to a solution of FCAT followed by addition of negatively charged **2**. The resulting solid was separated from the reaction solution, washed three times with deionized water (Figure S19) and stored in water at 4 °C. We examined the crystallinity of the product by performing powder X-ray diffraction (PXRD) experiments (Figure S3 and S26). Inspection of the PXRD pattern showed peaks characteristic of BioHOF-1 at 2θ values of 8.6°, and 17.4°, indicating that the HOF forms in the presence of the enzyme (Figure S3 and S26). Next, we em-

ployed confocal laser scanning microscopy (CLSM) to visualize the spatial distribution of FCAT within the HOF-based biocomposites. For comparison, we also synthesized FCAT-on-BioHOF-1 by mixing FCAT with pre-synthesized BioHOF-1 crystals in water. Figures 1c, S4, and S5 show a clear difference between the CLSM images of FCAT-on-BioHOF-1 and FCAT@BioHOF-1. As expected, the FCAT molecules were distributed homogeneously within the FCAT@BioHOF-1 crystals, which is consistent with enzyme encapsulation. Conversely, the images of FCAT-on-BioHOF-1 show greater fluorescence intensity on the crystal surfaces. The loading of FCAT in FCAT@BioHOF-1 was determined to be 6.0 ± 0.5 wt% by ICP-MS.[41] The incorporation of FCAT into the composite is also supported by solid-state UV-visible spectroscopy data that show the Soret absorption band at 407 nm ($\pi$-$\pi^*$), due to the iron-heme cofactor in CAT (Figure S9).[42] Furthermore, the congruence of the Soret absorption peak in free FCAT and FCAT@BioHOF-1 is indicative that the encapsulation process did not lead to significant structural changes at the enzyme active site.[42]

Gas adsorption isotherm experiments (77K $N_2$) indicated that activated samples of FCAT@BioHOF-1 were non-porous to $N_2$. In addition, the parent HOF is also non-porous to $N_2$. These data are consistent with our previous results for amidinum-carboxylate-based HOFs and may be attributed to the loss of structurally important water molecules upon activation.[33] We then turned our efforts to evaluating the accessible porosity of the HOF in solution via fluorescein dye adsorption. The molecular shape of fluorescein can be described as an oblate spheroid with semi-axes of 2 and 7 Å[43], thus we anticipated that it should diffuse through the pore network of the HOF (crystallographically determined pore apertures of 6.4 Å, Figure S1). We exposed the HOF crystals to fluorescein for 4 hours and then collected CLSM images to identify where the dye was spatially located within the crystals. Close inspection of the images shows that fluorescein is homogeneously distributed throughout the HOF (Figure S10), thus confirming solution accessible porosity. In addition, we carried out analogous solution adsorption experiments for ZIF-8, ZIF-90 and MAF-7 which all have reported crystallographic pore network apertures of ~3.4 Å (note that rotation of the imidazolate rings of ZIF-8 can allow molecules of ~5.0 Å to access the pores).[44] Even after soaking in fluorescein solution for 24 hrs, the CLSM images show that the dye is located only on the surface of each of the ZIF crystals (Figure S10). In summary, these experiments confirm that the HOF pores are accessible to guests in solution and highlight that the larger pore apertures, with respect to ZIF-8, ZIF-90 and MAF-7, allow for the exploration of an expanded number of enzyme substrates.

Next we compared the rate of $H_2O_2$ decomposition catalyzed by free FCAT and FCAT@BioHOF-1 in a variety of conditions. The $H_2O_2$ decomposition rate ($V_{obs}$) was quantified via the FOX assay. As a control experiment, we confirmed that neat BioHOF-1 crystals do not catalyze the decomposition of $H_2O_2$ (Figure S21). Conversely, when exposed to $H_2O_2$, at room temperature and pH 8 FCAT@BioHOF-1 retained activity ($V_{obs}$ = 0.28 μM $\mu g_{FCAT}^{-1}$ $s^{-1}$, Figure S22). Given this positive result, we assessed the capacity of the HOF coating to protect CAT over the pH range 5-10 as it is known that the optimal activity for free CAT is at pH of 7-8.[45] Figures 2a and S22 show the optimal activity for the biocomposite is significantly broadened, indeed, >90% of the maximum activity is retained for FCAT@BioHOF-1 operating over the biologically-relevant pH range 5-10. To confirm that the HOF retains porosity over a pH range 5-10 via fluorescein dye adsorption (Figure S11), HOF crystals were exposed to pH 5 and pH 10 solutions for 30 min, respectively. Next the respective samples were treated with fluorescein and CLSM images were collected. Figure S11 shows that in both cases the dye adsorbed homogeneously within the pore network indicating that the HOF remains porous after these treatments. Further, PXRD and Raman, UV-visible and FTIR spectroscopic analyses show that the HOF is structurally stable at low pH values (Figure S12-S17). In contrast, ZIF-8 degrades even in mildly acidic conditions and phosphate buffer solutions (Figure S14-S16).[21, 22] These results represent a notable advantage of HOF-based biocomposites for applications where stability is needed in acidic conditions. However, we note that under extremely basic conditions, pH 14, the HOF materials degrade while ZIF-8 retains structural integrity (Figure S18).

Many enzymes are also sensitive to elevated temperatures. Thus, we assessed the enzymatic activity of free FCAT and FCAT@BioHOF-1 after heating at 60 °C for 30 min. The activities are shown in Figure 2b and S23 relative to the activity of a control experiment carried out at room temperature (RT, 25 ± 1 °C). Free FCAT rapidly lost activity from *ca.* 1.23 μM $\mu g_{FCAT}^{-1}$ $s^{-1}$ at RT to 0.02 μM $\mu g_{FCAT}^{-1}$ $s^{-1}$ after exposure to 60 °C temperatures for 30 min (Figure 2b and S23). However, the BioHOF-1 coating significantly enhanced the thermostability of the encapsulated enzyme maintaining *ca.* 79% of its initial activity after 30 min at 60 °C (Figure 2b).

Next, we sought to establish the activites of encapsulated, and surface absorbed, enzyme after exposure to trypsin (a proteolytic agent) and urea (a chaotropic agent). Thus, we synthesized FCAT@BioHOF-1, FCAT-on-BioHOF-1 and treated these materials, along with FCAT, with both trypsin and urea, respectively. Enzymatic activity and structural characterizations are reported in Figure S24-S29. Trypsin is a proteolytic enzyme that due to its size (approximated as an ellipsoid with dimensions of 4.8 × 3.7 × 3.2 nm)[46] can only access surface bound and not the embedded enzyme. Subsequent to trypsin exposure, FCAT is completely deactivated whilst the activity of the surface bound FCAT (FCAT-on-BioHOF-1) is significantly reduced (*ca.* 80% loss of its original biological activity, Figure 2b, S24, and S28). However, FCAT@BioHOF-1 retains 76% of its original activity (Figure 2b and S24). These data clearly show that the enzyme retains activity post-encapsulation and surface adsorption effects are not solely responsible for the protection observed. Next we exposed FCAT@BioHOF-1, FCAT-on-BioHOF-1 and free

FCAT to urea; a small molecule that engenders protein unfolding and loss of activity.[47] After treating FCAT and FCAT-on-BioHOF-1 with urea a significant loss in the activities was observed (*ca.* 90% and 70% of the original activity was loss for FCAT and FCAT-on-BioHOF-1, respectively; Figure 2b, S25, and S28). However, FCAT@BioHOF-1 retains *ca.* 75% activity (Figure 2b and S25). Given that urea is small enough to diffuse within the HOF pore network these data suggests that the microenvironment that houses the enzyme prevents unfolding[48] Presumably this occurs via tight encapsulation and/or protein-surface interactions.[8, 48] Lastly, we performed ten catalysis/filtration cycles using FCAT@BioHOF-1 to assess the catalytic durability of the biocomposite. Figure S30 and S31 show that cycling does not leads to an appreciable reduction in enzymatic activity or loss of crystallinity. In addition, the supernatant of the FCAT@BioHOF-1 composite showed negligible enzymatic activity which suggests that enzyme leaching is minimal (Figure S21).

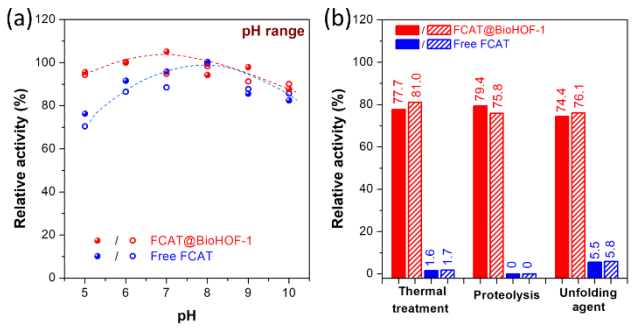


**Figure 2**. (a) Relative activity of free FCAT (blue) and FCAT@BioHOF-1 (red) at different pH (Figure S22). Individual data points from (duplicate experiments) are shown as open and closed circles.[49] (b) Relative activity (%) of free FCAT and FCAT@BioHOF-1 after thermal treatment (60°C for 30 min), and exposure to trypsin (2 mg $mL^{-1}$ for 120 min) and urea (6 M urea for 30 min). Individual data points from (duplicate experiments) are shown as filled and shaded bars.[49]

To examine the scope of this encapsulation strategy we examined the activites of HOF-based biocomposites of alcohol oxidase (AOx). AOx is an enzyme that consists of eight identical subuinits (diameter = 20 nm by electron microscopy[50] or 15 nm by DLS (Table S1)) and catalyzes the oxidation of short aliphatic alcohols to formaldehyde with concomitant production of $H_2O_2$.[51] Notably, FAOx@ZIFx and FAOx-on-ZIFx (ZIFx = ZIF-8, ZIF-90, and MAF-7) biocomposites synthesized in this work showed no activity (The synthesis, characterization, and catalytic performance of the FAOx/ZIFs biocomposites are shown section S8 of the SI (Figure S32-S37). We synthesized FAOx@BioHOF-1 (FAOx = fluorescein tagged AOx) composites (Figure S41) with an enzyme loading of 2.9 ± 0.6 wt% and then assessed the activity of composite. The CLSM measurments of FAOx@BioHOF-1 (Figure 3a and S6) suggest a homogeneous distribution of the FAOx in the HOF crystals; however, in case of FAOx-on-BioHOF-1 the FAOx localize on the HOF surface (Figure S7). FAOx@BioHOF-1 retained *ca.* 60% of the activity of free FAOx (*ca.* 3.5 and 2.1 µM $\mu g_{FAOx}^{-1}$ $min^{-1}$ for free FAOx and FAOx@BioHOF-1, respectively) (Figure S39). The moderately lower observed rate for the encapsulated enzyme is may result from a variety of factors inherent and common to immobilization processes.[52, 53] Given that FAOx@BioHOF-1 was enzymatically active, we examined the HOF's protective capacity when composites were exposed to elevated temperature, trypsin and urea. Notably, the BioHOF-1 coating offered significant protection to the embedded enzyme compared to free FAOx (Figure 3b). In summary, the composite maintained *ca.* 85% of its original activity after heating at 60°C (compared to 20% for the free enzyme); *ca.* 70% after exposure to trypsin (compared to 14% for the free enzyme); and, *ca.* 71% after exposure to urea (compared to 15% for the free enzyme) (Figure 3b and S38, S40-S44). These results exemplify how the scope of enzyme encapsulation in crystalline frameworks can be expanded using BioHOF-1.

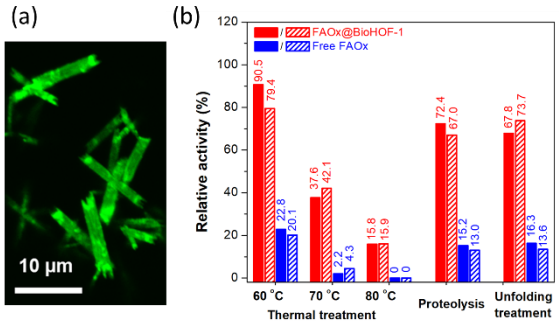


**Figure 3**. (a) CLSM image of the FAOx@BioHOF-1 (b) Relative activity (%) of free FAOx and FAOx@BioHOF-1 after heating (60, 70, and 80 °C for 10 min) and exposure to trypsin (2 mg $mL^{-1}$ for 2 h) and urea (6 M urea for 30 min Individual data points from (duplicate experiments) are shown as filled and shaded bars.[49]

Lastly, we carried out small angle X-ray scattering (SAXS) experiments to examine the kinetics of protein@BioHOF-1 formation and to determine if a hierarchical pore structure was present. We previously employed this technique to show that the growth of ZIF-8 was induced by the presence of bovine serum albumin (BSA) in solution and that the BSA@ZIF-8 structure possessed pores large enough to accommodate the protein.[8] As such, we used BSA as a model protein in this study so we could compare the data with that obtained for the BSA@ZIF-8. Time-resolved SAXS experiments were performed using a stop-flow setup[54, 55] and the kinetics of the nucleation, growth and crystallization of HOF particles (time resolution 100 ms) were monitored in the presence and absence of bovine serum albumin (BSA). Our data show that nuclei formed within the first 100 ms with or without the addition of BSA. Subsequently, in both cases, the nuclei form amorphous particles which crystallize within 100 s. This interpretation is supported by monitoring the intensity of the (110) diffraction peak of BioHOF-1 at 6.1 $nm^{-1}$ (Figure S45). After 50 s of mixing, the (110) diffraction peak of BioHOF-1 could be clearly observed and increased in in-

tensity until it reached a maximum after *ca.* 200 s. These experiments suggest that on time scales > 100 ms, HOF growth is not influenced by the presence of BSA and that encapsulation occurs *via* particle aggregation. SAXS can also be employed to ascertain the presence of a hierarchical pore structure in the HOF-based composites. After 15 min of growth we fitted the SAXS patterns with a hierarchical structural model of the neat HOF and BSA@BioHOF-1 (Figure 4 and S46, and S48). The BSA@BioHOF-1 data fit showed the presence of mesopores with a radius of gyration ($R_g$) of 4.9 ± 0.5 nm (Figure 4), that are sufficiently large to accommodate isolated BSA molecules ($R_g$ =3.02 nm[56]). Conversely, the data for the pure HOF shows an absence of mesopores (Figure S48).

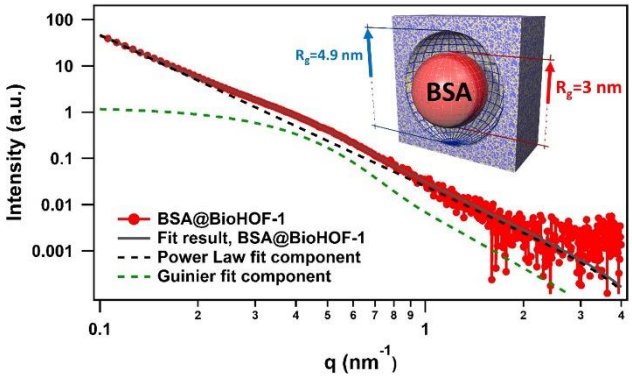


Figure 4. Fitted SAXS patterns together with the single-components of the fit (Power Law and Guinier knee components)[57, 58] of BSA@BioHOF-1 after 700 s of growth. Inset shows the gyration radius (arrows) of BSA and the observed mesopore in the BSA@BioHOF-1.

## CONCLUSIONS

Herein, we showed that a water stable amidinium/carboxylate-based HOF can encapsulate biomacromolecules and form a porous, crystalline coating that offers protection from conditions that would typically lead to loss of their native activity. In contrast to ZIF-8, the HOF-based biocomposites possess larger pore apertures and are stable towards acidic pH and phosphate buffers. Furthermore, the HOF coating retains the activity and protects the enzyme FAOx in challenging conditions, whereas ZIF-based composites of FAOx do not show activity. Accordingly, HOFs represent a new class of modular, crystalline materials poised for further exploration in the area of biomolecule protection.

## EXPERIMENTAL SECTION

### Syntheses

All chemicals and solvents were purchased from commercial sources and were used as received without further purification. The tetrahedral amidinium precursor **1**·$Cl_4$ was prepared as previously described.[33]

### Fluorescein-tagged enzyme

Fluorescein isothiocyanate (FITC, 0.5 mg) and catalase (CAT; Sigma-Aldrich, catalase from bovine liver, 2000-5000 units mg$^{-1}$ protein, 40 mg) were dissolved in a carbonate-bicarbonate aqueous buffer solution (0.1 M, pH 9.2, 4 mL) and left for two hours in darkness at room temperature under gentle stirring. The FITC-tagged CAT (FCAT) was recovered by passing the reaction mixture through an Illustra NAP-25 column (GE Healthcare Life Sciences, NSW, Australia). The crude FCAT solution was concentrated through a 10 K membrane by centrifugation (4000 rpm for 20 min), followed by solvent-exchange with ultrapure water. The concentration-solvent-exchange process was repeated two times to ensure the buffer salts were completely removed from the solution. Thereafter, the concentrated FCAT aqueous solution was passed through a NAP-25 column again to ensure the complete removal of unreacted FITC. The obtained FCAT solution was stored in darkness at 4 °C.

A similar method was used to prepare fluorescein-tagged alcohol oxidase (FAOx, Sigma-Aldrich, alcohol oxidase solution from *Pichia pastoris,* buffered aqueous solution, 10-40 units/mg protein).

### Synthesis of BioHOF-1

Amidinium compound **1**·$Cl_4$ (4 mg), was dissolved in $H_2O$ (1 mL) to form solution A. Carboxylate compound $H_4$**2** (3 mg) was dispersed in Milli-Q $H_2O$ (950 µL) , followed by the addition of aqueous ammonium hydroxide solution (1% v/v, 50 µL) to deprotonate 2 (solution B). Thereafter, solution B was added to solution A under stirring conditions at room temperature.[34] Precipitates were formed immediately upon mixing (Figure S47). The reaction mixture was left to gently stir in the dark for 1 h. The BioHOF-1 material was then recovered by centrifugation, and then washed, dispersed, and centrifuged three times in Milli-Q $H_2O$ to remove any unreacted precursors.

### Synthesis of the FCAT@BioHOF-1 biocomposite

**1**·$Cl_4$ (4 mg) was dissolved in $H_2O$ (0.5 mL) to form solution A. An aqueous solution of FCAT (1 mg, 0.5 mL of 2 mg mL$^{-1}$ stock solution) was added to solution A and stirred at room temperature for 10 min to form solution B. $H_4$**2** (3 mg) was dissolved in 0.95 mL of $H_2O$ and 0.05 mL of 1% $NH_4OH$ to form solution C. Solution C was then added dropwise to solution B under stirring. The mixture was then left to gently stir for another 1 h to ensure the completion of the synthesis. Thereafter, the FCAT@BioHOF-1 composite was collected by centrifugation and then washed, dispersed, and centrifuged three times in Milli-Q $H_2O$ to remove any unreacted precursors and loosely adsorbed FCAT (Figure S19).

### Synthesis of the FAOx@BioHOF-1 biocomposite

**1**·$Cl_4$ (4 mg) was dissolved in $H_2O$ (0.75 mL) to form Solution A. An aqueous solution of FAOx (0.5 mg, 0.25 mL of 2 mg mL$^{-1}$ stock solution) was added to solution A and stirred at room temperature for 10 min to form solution B. $H_4$**2** (3 mg) was dissolved in 0.95 mL of $H_2O$ and 0.05 mL of 1% $NH_4OH$ to form solution C. Aliquots of solution C (20 µL) were then added to solution B under gentle stirring every 20 s. The mixture was gently stirred for an additional 1 h to ensure the completion of the synthesis. Thereafter, the FAOx@BioHOF-1 composite was collected by centrifugation and then washed, dispersed, and centri-

fuged three times in Milli-Q $H_2O$ to remove any unreacted precursors and loosely adsorbed FAOx (Figure S19).

**Characterization**

**Powder X-ray diffraction (PXRD)**

PXRD patterns were obtained using a D4 ENDEAVOR X-ray Diffractometer from Bruker. A Co anode was used to produce $K_\alpha$ radiation ($\lambda$ = 1.78897 Å). Flat plate diffraction data was collected over the range $2\theta$ = 5–40 °. The PXRD data were modified by PowDLL Converter (version 2.68.0.0) and expressed as the copper-source irradiated patterns ($\lambda$ = 1.54056 Å).

**Confocal laser scanning microscopy (CLSM)**

The presence and spatial location of the fluorophore-tagged biomolecules in (or on) the composites was determined using CLSM technique (Olympus FV3000 Confocal Laser Scanning Microscope, OLYMPUS). The fluorescein-tagged biomolecules were excited at 488 nm and the fluorescence signal was collected in a window from 495 to 545 nm.

**Scanning electron microscopy (SEM)**

SEM images were collected using a Philips XL30 Field Emission Scanning Electron Microscope (FESEM). Prior to analysis, the samples were dispersed in ethanol by sonication, drop-cast on an aluminum SEM stage (12 mm), and sputter-coated with platinum to form a thin film (5 nm).

**Inductively Coupled Plasma Mass Spectrometer (ICP-MS)**

ICP-MS was performed on an Agilent 8900x QQQ-ICP-MS. The free enzyme or enzyme@BioHOF-1 composites (approximately 1 mg) were dispersed in a solution of $HNO_3$/HCl (0.25 mL of 70% $HNO_3$ (Ajax) and 0.25 mL of 37% HCl (Chem Supply)) and stored in Eppendorf tubes at room temperature overnight. The mixture was then centrifuged to remove any particulates in the supernatant. Thereafter, the clear supernatant (0.4 mL) was diluted to a final volume of 5 mL with Milli-Q $H_2O$ for ICP-MS analysis. The amount of enzyme within the sample was calculated according to a standard calibration curve for sulfur (prepared from sulfur standard solution from Sigma-Aldrich, Sulfur Standard for ICP (TraceCERT®, 1000 mg/L S in $H_2O$)).

**Synchrotron Small Angle X-ray Scattering**

Time-resolved SAXS data was collected on the SAXS beamline at the ELETTRA synchrotron light source.[54] Operation occurred at a photon energy of 8 keV covering the range of momentum transfer, $q = 4\pi \sin(\theta)/\lambda$, between 0.1 and 7.7 $nm^{-1}$. The kinetics of the MOF nucleation and growth was monitored using a commercial stopped flow apparatus SFM-4 (Bio-Logic, Grenoble, France) especially designed for synchrotron radiation SAXS investigations. Two independently controlled syringes were filled with the carboxylate ligand solution and the amidinium ligand (or amidinium ligand + BSA) solution, respectively. Upon triggering by the data acquisition system, the two syringe volumes were mixed and injected into a quartz capillary (1 mm) placed in the X-Ray beam (the mixing/injection process lasts a few ms). The volume ratio between the two solutions and their concentration was set to replicate the conditions used for the syntheses in batch.

A total volume of 900 µL was injected for each experiment. Images were taken with a time resolution of 100 ms (detector: Pilatus3 1M, Dectris Ltd, Baden, Switzerland; sample to detector distance: 1260 mm, as determined with a silver behenate calibration sample). All experiments were performed at room temperature. The resulting two-dimensional images were radially integrated to obtain a 1D pattern of normalized intensity versus scattering vector q. The background was collected using MilliQ $H_2O$ and subtracted as background from the normalized data.

**Dynamic light scattering (DLS) and zeta potential measurements**

BSA, FCAT, or FAOx (1 mg) was dissolved in 1 mM PBS buffer (pH 7.4, 1 ml). Thereafter, 20 µL aqueous solution of **1** or **2** (deprotonated using 1% $NH_4OH$) was introduced into the protein solution. DLS and zeta potentials for the pure protein or protein/ligand samples were obtained on a Malvern ZetaSizer dynamic light scattering instrument using a Quartz cuvettes (DTS2145) and folded capillary zeta potential cell (DTS1070), respectively, at 25 °C.

**Catalytic performance of FCAT and the FCAT@BioHOF-1 composites**

The Ferrous Oxidation in Xylenol orange (FOX) assay was applied to quantify the concentration of $H_2O_2$ (Figure S20).[59] FCAT or the FCAT@BioHOF-1 composite was added into phosphate buffer (100 mM, pH 8, 0.2 mL). Thereafter, $H_2O_2$ stock solution (1 mM in $H_2O$, 0.15 mL) was added. The volume of the reaction mixture was adjusted to 1 mL by $H_2O$. The catalyst dosage (based on FCAT) in the enzymatic reactions were 2.6 and 2.9 µg for FCAT and FCAT@BioHOF-1, respectively (determined by ICP-MS). At different time intervals, aliquots of the mixtures (50 µL) were sampled and mixed with FOX reagent (950 µL) in an Eppendorf tube and then incubated for at least 30 min at room temperature. After incubation, the samples were centrifuged. The UV–visible absorbances at 560 nm for the supernatant were recorded to calculate the $H_2O_2$ concentration. The reaction rate ($V_{obs}$, mM $s^{-1}$) is defined as the initial $H_2O_2$ decomposition velocity of the enzymatic assay.

**Catalytic performance of FAOx and FAOx@BioHOF-1 composites**

The enzymatic activity of FAOx and the FAOx@BioHOF-1 composite were measured according to a modified protocol from Sigma-Aldrich. One tablet of 2,2′-azino-*bis*-(3-ethylbenzothiazoline-6-sulfonic acid) (ABTS, Sigma-Aldrich, 10 mg substrate per tablet) was dissolved in potassium phosphate buffer (pH 7.5, 0.1 M, 10 mL) to form solution A. Oxygen gas was bubbled through solution A for ~5 minutes before use. Solution B (~250 units $mL^{-1}$ of peroxidase solution) was prepared by dissolving 1.7 mg of HRP (Sigma-Aldrich, 148 units $mg^{-1}$) in Milli-Q $H_2O$ (1 mL). In a typical assay test, solution A (1 mL), Milli-Q $H_2O$ (1.8 mL), solution B (0.01 mL), and aqueous methanol solution (methanol (0.1 mL) in Milli-Q $H_2O$ (1 mL), 0.1

mL) were mixed in a cuvette (light path = 1 cm) under magnetic stirring. Thereafter, free FAOx or FAOx@BioHOF-1 stock solution (0.1 mL) was introduced and the reaction mixture was monitored continuously at 405 nm under stirring conditions. The reaction rate was determined using the maximum linear rate of the increase of $A_{405}$.

In the total reaction mixture (3.01 mL), the final chemical concentrations are: potassium phosphate (33 mM), 0.66 mM ABTS (0.66 mM), aqueous methanol (0.033% (v/v)), and HRP (2.5 units). The generation of $H_2O_2$ in the system was calculated according to the formation of oxidized ABTS in the system (ABTS, extinction coefficient at 405 nm = 36.8 $mM^{-1}$ $cm^{-1}$).

## ASSOCIATED CONTENT

**Supporting Information**. Information related to synthesis of the biocomposites, additional experimental and analytical detail for the biocomposites. This material is available free of charge *via* the Internet at http://pubs.acs.org.

## AUTHOR INFORMATION


### Corresponding Authors

*Email: christian.doonan@adelaide.edu.au; paolo.falcaro@tugraz.at; nicholas.white@anu.edu.au; christopher.sumby@adelaide.edu.au


### Author Contributions

W. L. and F. C. contribute equally to the article. All authors have given approval to the final version of the manuscript.


### Funding Sources

Australian Research Council Discovery Project (DP170103531) and Discovery Early Career Research Award (DE170100200).


### Notes

The authors declare no competing financial interest.

## ACKNOWLEDGMENT


This work was supported by the Australian Research Council (DP170103531 and DE170100200). PF acknowledges LP-03.


## REFERENCES


1. Bommarius, A. S.; Paye, M. F., *Stabilizing biocatalysts*. *Chem. Soc. Rev.* **2013,** 42, 6534-6565.
2. Sheldon, R. A.; Brady, D., *The limits to biocatalysis: pushing the envelope*. *Chem. Commun.* **2018,** 54, 6088-6104.
3. Hudson, S.; Cooney, J.; Magner, E., *Proteins in Mesoporous Silicates*. *Angew. Chem. Int. Ed.* **2008,** 47, 8582-8594.
4. Drout, R. J.; Robison, L.; Farha, O. K., *Catalytic applications of enzymes encapsulated in metal–organic frameworks*. *Coord. Chem. Rev.* **2019,** 381, 151-160.
5. Sun, Q.; Fu, C.-W.; Aguila, B.; Perman, J.; Wang, S.; Huang, H.-Y.; Xiao, F.-S.; Ma, S., *Pore Environment Control and Enhanced Performance of Enzymes Infiltrated in Covalent Organic Frameworks*. *J. Am. Chem. Soc.* **2018,** 140, 984-992.
6. Lyu, F.; Zhang, Y.; Zare, R. N.; Ge, J.; Liu, Z., *One-Pot Synthesis of Protein-Embedded Metal–Organic Frameworks with Enhanced Biological Activities*. *Nano Lett.* **2014,** 14, 5761-5765.
7. Shieh, F.-K.; Wang, S.-C.; Yen, C.-I.; Wu, C.-C.; Dutta, S.; Chou, L.-Y.; Morabito, J. V.; Hu, P.; Hsu, M.-H.; Wu, K. C. W.; Tsung, C.-K., *Imparting Functionality to Biocatalysts via Embedding Enzymes into Nanoporous Materials by a de Novo Approach: Size-Selective Sheltering of Catalase in Metal–Organic Framework Microcrystals*. *J. Am. Chem. Soc.* **2015,** 137, 4276-4279.
8. Liang, K.; Ricco, R.; Doherty, C. M.; Styles, M. J.; Bell, S.; Kirby, N.; Mudie, S.; Haylock, D.; Hill, A. J.; Doonan, C. J.; Falcaro, P., *Biomimetic mineralization of metal-organic frameworks as protective coatings for biomacromolecules*. *Nat. Commun.* **2015,** 6, 7240.
9. Liang, K.; Coghlan, C. J.; Bell, S. G.; Doonan, C. J.; Falcaro, P., *Enzyme encapsulation in zeolitic imidazolate frameworks: a comparison between controlled co-precipitation and biomimetic mineralisation*. *Chem. Commun.* **2016,** 52, 473-476.
10. Chen, W.-H.; Vázquez-González, M.; Zoabi, A.; Abu-Reziq, R.; Willner, I., *Biocatalytic cascades driven by enzymes encapsulated in metal–organic framework nanoparticles*. *Nat. Catal.* **2018,** 1, 689-695.
11. Liu, J.; Liu, T.; Du, P.; Zhang, L.; Lei, J., *Metal–Organic Framework (MOF) Hybrid as a Tandem Catalyst for Enhanced Therapy against Hypoxic Tumor Cells*. *Angew. Chem. Int. Ed.* **2019,** 58, 7808-7812.
12. Li, S.; Dharmarwardana, M.; Welch, R. P.; Ren, Y.; Thompson, C. M.; Smaldone, R. A.; Gassensmith, J. J., *Template-Directed Synthesis of Porous and Protective Core–Shell Bionanoparticles*. *Angew. Chem. Int. Ed.* **2016,** 55, 10691-10696.
13. Li, S.; Dharmarwardana, M.; Welch, R. P.; Benjamin, C. E.; Shamir, A. M.; Nielsen, S. O.; Gassensmith, J. J., *Investigation of Controlled Growth of Metal–Organic Frameworks on Anisotropic Virus Particles*. *ACS Appl. Mater. Interfaces* **2018,** 10, 18161-18169.
14. Luzuriaga, M. A.; Welch, R. P.; Dharmarwardana, M.; Benjamin, C. E.; Li, S.; Shahrivarkevishahi, A.; Popal, S.; Tuong, L. H.; Creswell, C. T.; Gassensmith, J. J., *Enhanced Stability and Controlled Delivery of MOF-Encapsulated Vaccines and Their Immunogenic Response In Vivo*. *ACS Appl. Mater. Interfaces* **2019,** 11, 9740-9746.
15. Wu, X.; Hou, M.; Ge, J., *Metal–organic frameworks and inorganic nanoflowers: a type of emerging inorganic crystal nanocarrier for enzyme immobilization*. *Catal. Sci. Technol.* **2015,** 5, 5077-5085.
16. Doonan, C.; Riccò, R.; Liang, K.; Bradshaw, D.; Falcaro, P., *Metal–Organic Frameworks at the Biointerface: Synthetic Strategies and Applications*. *Acc. Chem. Res.* **2017,** 50, 1423-1432.
17. Riccò, R.; Liang, W.; Li, S.; Gassensmith, J. J.; Caruso, F.; Doonan, C.; Falcaro, P., *Metal–Organic Frameworks for Cell and Virus Biology: A Perspective*. *ACS Nano* **2018,** 12, 13-23.
18. Du, Y.; Gao, J.; Zhou, L.; Ma, L.; He, Y.; Zheng, X.; Huang, Z.; Jiang, Y., *MOF-Based Nanotubes to Hollow Nanospheres through Protein-Induced Soft-Templating Pathways*. *Adv. Sci.* **2019,** 6, 1801684.
19. Eum, K.; Jayachandrababu, K. C.; Rashidi, F.; Zhang, K.; Leisen, J.; Graham, S.; Lively, R. P.; Chance, R. R.; Sholl, D. S.; Jones, C. W.; Nair, S., *Highly Tunable Molecular Sieving and Adsorption Properties of Mixed-Linker Zeolitic Imidazolate Frameworks*. *J. Am. Chem. Soc.* **2015,** 137, 4191-4197.
20. Zhang, H.; Hou, J.; Hu, Y.; Wang, P.; Ou, R.; Jiang, L.; Liu, J. Z.; Freeman, B. D.; Hill, A. J.; Wang, H., *Ultrafast selective transport of alkali metal ions in metal organic frameworks with subnanometer pores*. *Sci. Adv.* **2018,** 4, eaaq0066.
21. Luzuriaga, M. A.; Benjamin, C. E.; Gaertner, M. W.; Lee, H.; Herbert, F. C.; Mallick, S.; Gassensmith, J. J., *ZIF-8 degrades in cell media, serum, and some—but not all—common laboratory buffers*. *Supramol. Chem.* **2019**, DOI: 10.1080/10610278.2019.1616089.
22. Velásquez-Hernández, M. d. J.; Ricco, R.; Carraro, F.; Limpoco, F. T.; Linares-Moreau, M.; Leitner, E.; Wiltsche, H.; Rattenberger, J.; Schröttner, H.; Frühwirt, P.; Stadler, E. M.; Gescheidt, G.; Amenitsch, H.; Doonan, C. J.; Falcaro, P., *Degradation*

*of ZIF-8 in phosphate buffered saline media*. *CrystEngComm* **2019,** 21, 4538-4544.
23. Sun, C.-Y.; Qin, C.; Wang, X.-L.; Yang, G.-S.; Shao, K.-Z.; Lan, Y.-Q.; Su, Z.-M.; Huang, P.; Wang, C.-G.; Wang, E.-B., *Zeolitic imidazolate framework-8 as efficient pH-sensitive drug delivery vehicle*. *Dalton Trans.* **2012,** 41, 6906-6909.
24. Luo, J.; Wang, J.-W.; Zhang, J.-H.; Lai, S.; Zhong, D.-C., *Hydrogen-bonded organic frameworks: design, structures and potential applications*. *CrystEngComm* **2018,** 20, 5884-5898.
25. Li, P.; He, Y.; Guang, J.; Weng, L.; Zhao, J. C.-G.; Xiang, S.; Chen, B., *A Homochiral Microporous Hydrogen-Bonded Organic Framework for Highly Enantioselective Separation of Secondary Alcohols*. *J. Am. Chem. Soc.* **2014,** 136, 547-549.
26. Li, P.; He, Y.; Zhao, Y.; Weng, L.; Wang, H.; Krishna, R.; Wu, H.; Zhou, W.; O'Keeffe, M.; Han, Y.; Chen, B., *A Rod-Packing Microporous Hydrogen-Bonded Organic Framework for Highly Selective Separation of C2H2/CO2 at Room Temperature*. *Angew. Chem. Int. Ed.* **2015,** 54, 574-577.
27. Lin, R.-B.; He, Y.; Li, P.; Wang, H.; Zhou, W.; Chen, B., *Multifunctional porous hydrogen-bonded organic framework materials*. *Chem. Soc. Rev.* **2019,** 48, 1362-1389.
28. Hisaki, I.; Xin, C.; Takahashi, K.; Nakamura, T., *Designing Hydrogen-Bonded Organic Frameworks (HOFs) with Permanent Porosity*. *Angew. Chem. Int. Ed.* **2019,** 58, 11160-11170.
29. Simard, M.; Su, D.; Wuest, J. D., *Use of hydrogen bonds to control molecular aggregation. Self-assembly of three-dimensional networks with large chambers*. *J. Am. Chem. Soc.* **1991,** 113, 4696-4698.
30. Russell, V. A.; Evans, C. C.; Li, W.; Ward, M. D., *Nanoporous Molecular Sandwiches: Pillared Two-Dimensional Hydrogen-Bonded Networks with Adjustable Porosity*. *Science* **1997,** 276, 575-579.
31. Yang, W.; Greenaway, A.; Lin, X.; Matsuda, R.; Blake, A. J.; Wilson, C.; Lewis, W.; Hubberstey, P.; Kitagawa, S.; Champness, N. R.; Schröder, M., *Exceptional Thermal Stability in a Supramolecular Organic Framework: Porosity and Gas Storage*. *J. Am. Chem. Soc.* **2010,** 132, 14457-14469.
32. Yamagishi, H.; Sato, H.; Hori, A.; Sato, Y.; Matsuda, R.; Kato, K.; Aida, T., *Self-assembly of lattices with high structural complexity from a geometrically simple molecule*. *Science* **2018,** 361, 1242-1246.
33. Morshedi, M.; Thomas, M.; Tarzia, A.; Doonan, C. J.; White, N. G., *Supramolecular anion recognition in water: synthesis of hydrogen-bonded supramolecular frameworks*. *Chem. Sci.* **2017,** 8, 3019-3025.
34. Boer, S., Morshedi, M., Tarzia, A, Doonan, C. J. , White, N. G., *Molecular Tectonics: node-and-linker building block approach to a family of hydrogen bonded frameworks*. *Chem. Eur. J.* **2019,** 25, 10006-10012.
35. Zhou, H.-C.; Long, J. R.; Yaghi, O. M., *Introduction to Metal–Organic Frameworks*. *Chem. Rev.* **2012,** 112, 673-674.
36. Furukawa, H.; Cordova, K. E.; O'Keeffe, M.; Yaghi, O. M., *The Chemistry and Applications of Metal-Organic Frameworks*. *Science* **2013,** 341, 1230444.
37. Tamames-Tabar, C.; Cunha, D.; Imbuluzqueta, E.; Ragon, F.; Serre, C.; Blanco-Prieto, M. J.; Horcajada, P., *Cytotoxicity of nanoscaled metal–organic frameworks*. *J. Mater. Chem. B* **2014,** 2, 262-271.
38. Grall, R.; Hidalgo, T.; Delic, J.; Garcia-Marquez, A.; Chevillard, S.; Horcajada, P., *In vitro biocompatibility of mesoporous metal (III; Fe, Al, Cr) trimesate MOF nanocarriers*. *Journal of Materials Chemistry B* **2015,** 3, 8279-8292.
39. Fita, I.; Rossmann, M. G., *The NADPH binding site on beef liver catalase*. *Proc. Natl. Acad. Sci.* **1985,** 82, 1604-1608.
40. Maddigan, N. K.; Tarzia, A.; Huang, D. M.; Sumby, C. J.; Bell, S. G.; Falcaro, P.; Doonan, C. J., *Protein surface functionalisation as a general strategy for facilitating biomimetic mineralisation of ZIF-8*. *Chem. Sci.* **2018,** 9, 4217-4223.
41. Pröfrock, D.; Prange, A., *Inductively Coupled Plasma–Mass Spectrometry (ICP-MS) for Quantitative Analysis in Environmental and Life Sciences: A Review of Challenges, Solutions, and Trends*. *Appl. Spectrosc.* **2012,** 66, 843-868.
42. Dong, X.; Fan, Y.; Yang, P.; Kong, J.; Li, D.; Miao, J.; Hua, S.; Hu, C., *Ultraviolet-visible (UV-Vis) and fluorescence spectroscopic investigation of the interactions of ionic liquids and catalase*. *Appl. Spectrosc.* **2016,** 70, 1851-1860.
43. Pu, Y.; Wang, W.; Dorshow, R. B.; Alfano, R. R., *Picosecond polarization spectroscopy of fluorescein attached to different molecular volume polymer influenced by rotational motion*. SPIE: 2012; Vol. 8258.
44. Verploegh, R. J.; Nair, S.; Sholl, D. S., *Temperature and Loading-Dependent Diffusion of Light Hydrocarbons in ZIF-8 as Predicted Through Fully Flexible Molecular Simulations*. *J. Am. Chem. Soc.* **2015,** 137, 15760-15771.
45. Chance, B., *Effect of pH upon the reaction kinetics of the enzyme-substrate compounds of catalse*. *J. Biol. Chem.* **1952,** 194, 471-481.
46. Saha, B.; Saikia, J.; Das, G., *Correlating enzyme density, conformation and activity on nanoparticle surfaces in highly functional bio-nanocomposites*. *Analyst* **2015,** 140, 532-542.
47. Bennion, B. J.; Daggett, V., *The molecular basis for the chemical denaturation of proteins by urea*. *Proc. Natl. Acad. Sci.* **2003,** 100, 5142-5147.
48. Liao, F.-S.; Lo, W.-S.; Hsu, Y.-S.; Wu, C.-C.; Wang, S.-C.; Shieh, F.-K.; Morabito, J. V.; Chou, L.-Y.; Wu, K. C. W.; Tsung, C.-K., *Shielding against Unfolding by Embedding Enzymes in Metal–Organic Frameworks via a de Novo Approach*. *J. Am. Chem. Soc.* **2017,** 139, 6530-6533.
49. Cumming, G.; Fidler, F.; Vaux, D. L., *Error bars in experimental biology*. *The Journal of Cell Biology* **2007,** 177, 7-11.
50. Zhang, H.; Loovers, H. M.; Xu, L.-Q.; Wang, M.; Rowling, P. J. E.; Itzhaki, L. S.; Gong, W.; Zhou, J.-M.; Jones, G. W.; Perrett, S., *Alcohol oxidase (AOX1) from Pichia pastoris is a novel inhibitor of prion propagation and a potential ATPase*. *Mol. Microbiol.* **2009,** 71, 702-716.
51. Ozimek, P.; Veenhuis, M.; van der Klei, I. J., *Alcohol oxidase: A complex peroxisomal, oligomeric flavoprotein*. *FEMS Yeast Res.* **2005,** 5, 975-983.
52. Hanefeld, U.; Gardossi, L.; Magner, E., *Understanding enzyme immobilisation*. *Chem. Soc. Rev.* **2009,** 38, 453-468.
53. Küchler, A.; Yoshimoto, M.; Luginbühl, S.; Mavelli, F.; Walde, P., *Enzymatic reactions in confined environments*. *Nat. Nanotechnol.* **2016,** 11, 409.
54. Amenitsch, H.; Rappolt, M.; Kriechbaum, M.; Mio, H.; Laggner, P.; Bernstorff, S., *First performance assessment of the small-angle X-ray scattering beamline at ELETTRA*. *J. Synchrotron Rad.* **1998,** 5, 506-508.
55. Grillo, I., *Applications of stopped-flow in SAXS and SANS*. *Curr. Opin. Colloid Interface Sci.* **2009,** 14, 402-408.
56. Pernot, P.; Round, A.; Barrett, R.; De Maria Antolinos, A.; Gobbo, A.; Gordon, E.; Huet, J.; Kieffer, J.; Lentini, M.; Mattenet, M.; Morawe, C.; Mueller-Dieckmann, C.; Ohlsson, S.; Schmid, W.; Surr, J.; Theveneau, P.; Zerrad, L.; McSweeney, S., *Upgraded ESRF BM29 beamline for SAXS on macromolecules in solution*. *J. Synchrotron Rad.* **2013,** 20, 660-664.
57. Aragón, S. R.; Pecora, R., *Theory of dynamic light scattering from polydisperse systems*. *J. Chem. Phys.* **1976,** 64, 2395-2404.
58. Kotlarchyk, M.; Chen, S. H., *Analysis of small angle neutron scattering spectra from polydisperse interacting colloids*. *J. Chem. Phys.* **1983,** 79, 2461-2469.
59. Ou, P.; Wolff, S. P., *A discontinuous method for catalase determination at 'near physiological' concentrations of H2O2*

*and its application to the study of H2O2 fluxes within cells. J. Biochem. Biophys. Methods* **1996,** 31, 59-67.

Authors are required to submit a graphic entry for the Table of Contents (TOC) that, in conjunction with the manuscript title, should give the reader a representative idea of one of the following: A key structure, reaction, equation, concept, or theorem, etc., that is discussed in the manuscript. Consult the journal's Instructions for Authors for TOC graphic specifications.

Insert Table of Contents artwork here

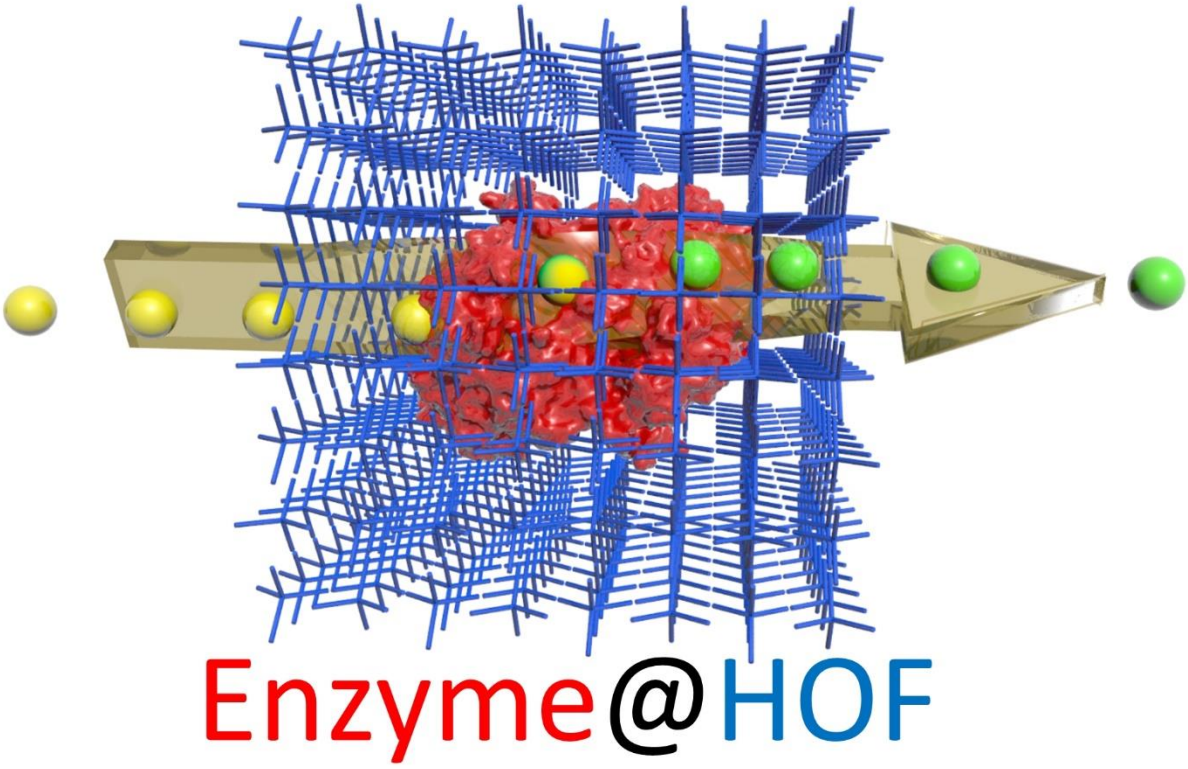

# Supplementary Information for:

# Enzyme Encapsulation in a Porous Hydrogen-Bonded Organic Framework

Weibin Liang[†▽], Francesco Carraro[§▽], Marcello B. Solomon[§], Stephen G. Bell[†], Heinz Amenitsch[‖], Christopher J. Sumby[†*], Nicholas G. White[‡*], Paolo Falcaro[§,†*], Christian J. Doonan[†*]

[†] Department of Chemistry and the Centre for Advanced Nanomaterials, The University of Adelaide, Adelaide, South Australia 5005, Australia

[§] Institute of Physical and Theoretical Chemistry, Graz University of Technology, Stremayrgasse 9, Graz 8010, Austria

[‖] Institute of Inorganic Chemistry, Graz University of Technology, Stremayrgasse 9, Graz 8010, Austria

[‡] Research School of Chemistry, The Australian National University, Canberra, ACT, Australia

[▽] These authors contribute equally to the article

**Table of Contents**

## S1. Structural description of the studied hydrogen-bonded organic framework (HOF, BioHOF-1)

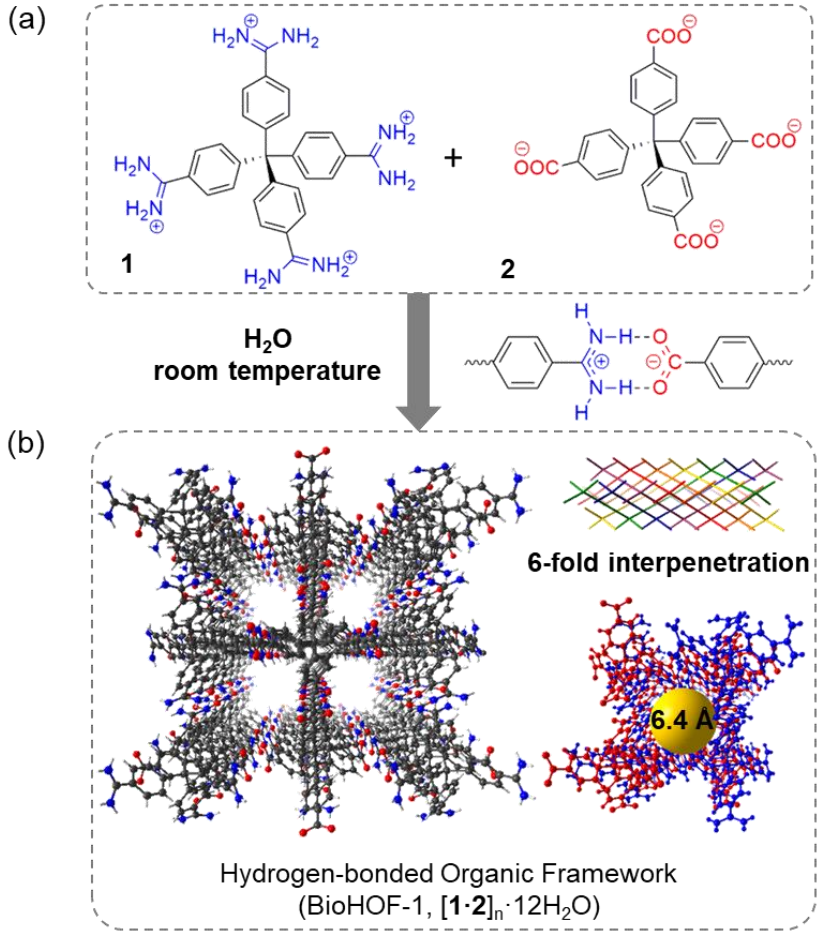


Figure S1. (a) Molecular structures of *tetrakis*(4-amidiniumphenyl)methane (**1**, blue) and *tetrakis*(4-carboxylphenyl)methane (**2**, red); (b) a representation of the Hydrogen-bonded Organic Framework (BioHOF-1, [**1**·**2**]$_n$·12$H_2O$) showing the arrangement of its molecular building blocks, 6-fold interpenetration and one-dimensional square-shaped pore channel (~6.4 Å). Solvent molecules are omitted for clarity.

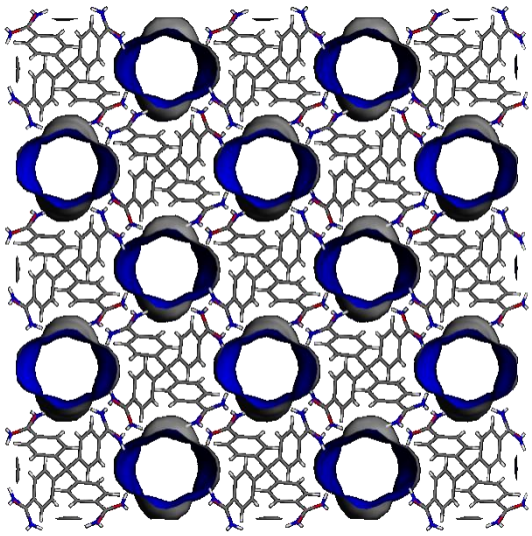

Figure S2. Connolly surface diagram of BioHOF-1 using $N_2$ as a probe molecule (probe radius 1.8 Å). The inner surfaces of the cavities have been shown in white, while the outer surfaces are represented in blue. The values of the theoretical pore volume and surface area for BioHOF-1 were calculated using Materials Studio to be 0.28 $cm^3\ g^{-1}$ and 2002.26 $m^2\ g^{-1}$, respectively.

## S2. Dynamic light scattering (DLS) and zeta potential measurements

Table S1. Volume-average hydrodynamic diameter ($D_h$) and zeta potential values for the protein and protein/BioHOF-1 ligand mixture.

| Sample | $D_h$ (nm) | Zeta potential (mV) |
|---|---|---|
| BSA[a] | 6.7 ± 0.1 | -11.2 ± 0.4 |
| BSA/1[b] | 7.3 ± 0.1 | 3.6 ± 0.1 |
| BSA/2[c] | 6.7 ± 0.1 | -10.9 ± 0.9 |
| FCAT[a] | 10.8 ± 1.0 | -15.8 ± 1.1 |
| FCAT/1[b] | 2050 ± 578.4[d] | 2.4 ± 0.2 |
| FCAT/2[c] | 10.8 ± 2.3 | -16.5 ± 0.5 |
| FAOx[a] | 15.0 ± 0.1 | -26.5 ± 0.4 |
| FAOx/1[b] | 3183 ± 535.1[d] | 1.9 ± 0.1 |
| FAOx/2[c] | 15.3 ± 0.4 | -28.5 ± 0.9 |

[a]1 mg of protein was dissolved in 1 mL of 1 mM pH 7.4 PBS buffer; [b]0.1 mg of 1 in 20 µL of $H_2O$ was added into and mix with the protein buffer solution in 1 mM pH 7.4 PBS buffer; [c]0.1 mg of 2 (deprotonated by 1% $NH_4OH$ aqueous solution) in 20 µL of $H_2O$ was added into and mix with the protein buffer solution in 1 mM pH 7.4 PBS buffer; [d]the high $D_h$ value and large standard deviation are due to protein aggregation.

In the case of the BioHOF-1 we surmized that a negative protein surface charge would accumulate the positively charged amidinium building blocks. Thus, we measured the zeta potential of BSA (-11.2 ± 0.4 mV), fluorescein-tagged catalase (FCAT) (-15.8 ± 1.1 mV) and fluorescein-tagged alcohol oxidase (FAOx) (-26.5 ± 0.4 mV) in PBS buffer to provide quantitative data. Given that the surface charge for each protein was negative, we posited that they would accumulate the positively charged amidinium functionalized building block at their surface in preference to the carboxylate based building block. Indeed DLS experiments (Table S1) confirm this hypothesis. For example, free BSA affords a diameter of 6.7 ± 0.1 nm that remains essentially unchanged when the negatively charged carboxylate functionalised building block is added to the solution (6.7 ± 0.1 nm). However, upon addition of the positively charged amidinium functionalized building block, the DLS experiments show that the diameter increases to 7.3 ± 0.1 nm. Likewise, for FCAT and FAOx, the diameters remain unchanged upon addition of the carboxylate building block. However, upon addition of the positively charged amidinium building block the diameter increases

dramatically *ca.* 2 orders of magnitude for both. These experiments confirm that the attractive forces between the oppositely charged HOF building block and protein surface give rise to an increase in particle size that could induce growth of the HOF biocomposites. We note that these experiments were carried out in PBS buffer so that constant pH was maintained and charge interactions could be studied directly. Nevertheless, the experiments point towards the important role that the charge of the organic building block and protein surface charge play in the synthesis of the HOF biocomposites. For example, for both FCAT and FAOx the amidinium building block may lead to the formation of aggregates that may give rise to increased stability.[1, 2]

## S3. Physical properties of FCAT@BioHOF-1 and FAOx@BioHOF-1 composites

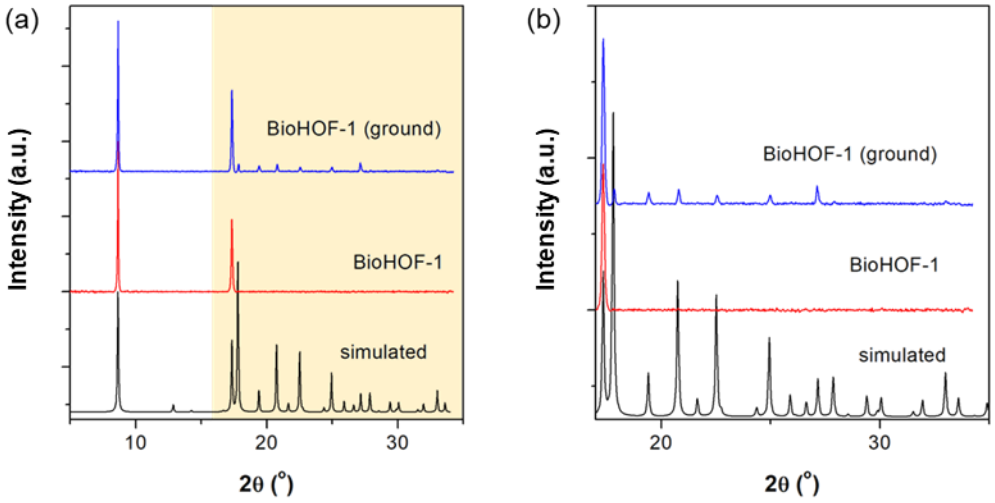


Figure S3. (a) Experimental powder X-ray diffraction patterns of the as-synthesized BioHOF-1; (b) the highlighted area (2θ = 17-35°) in Figure S3a. After grinding, other related peaks for BioHOF-1 appear indicating the preferred orientation effects in the as-synthesized sample. The simulated PXRD pattern for BioHOF-1 was generated from the single-crystal X-ray diffraction data.[3]

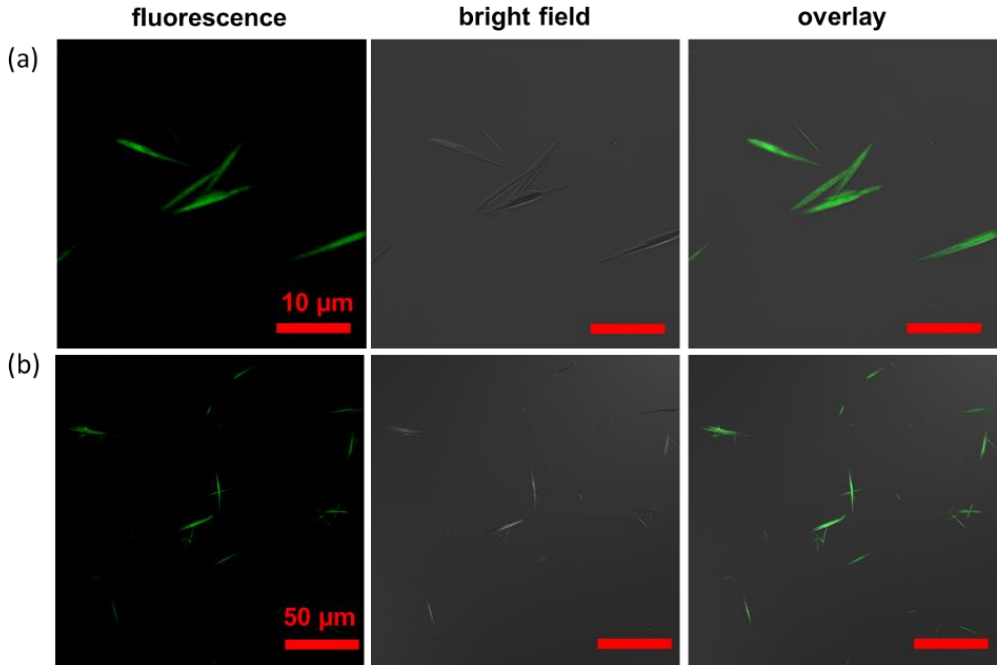


Figure S4. Confocal laser scanning micrographs showing the fluorescence (left), bright field (center), and overlay (right) images of FCAT@BioHOF-1 at two different magnifications.

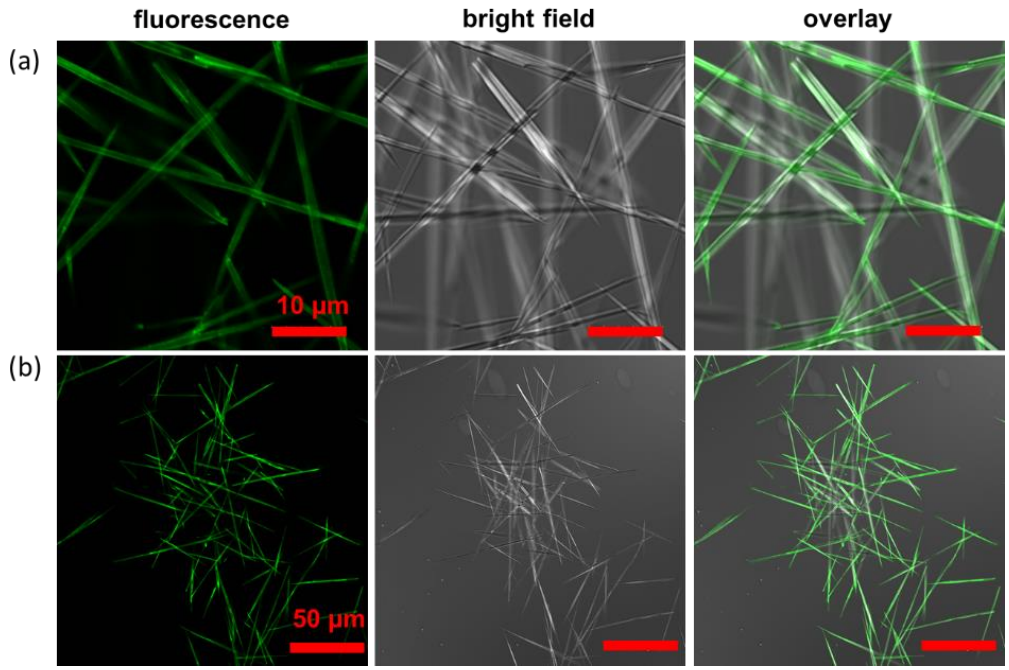


Figure S5. Confocal laser scanning micrographs showing the fluorescence (left), bright field (center), and overlay (right) images of FCAT-on-BioHOF-1 at two different magnifications.

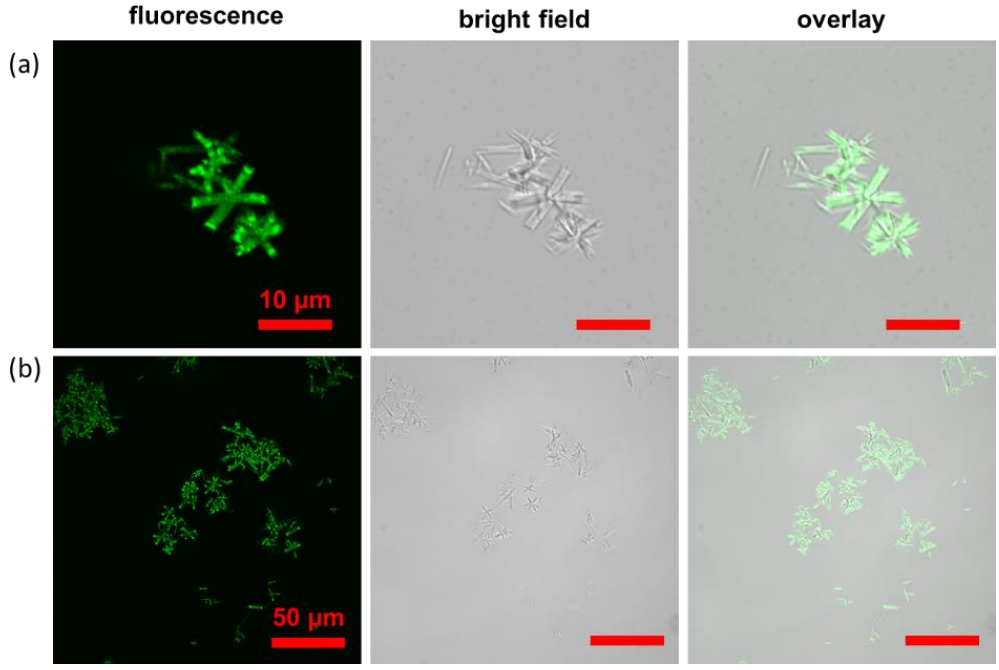


Figure S6. Confocal laser scanning micrographs showing the fluorescence (left), bright field (center), and overlay (right) images of FAOx@BioHOF-1 at two different magnifications.

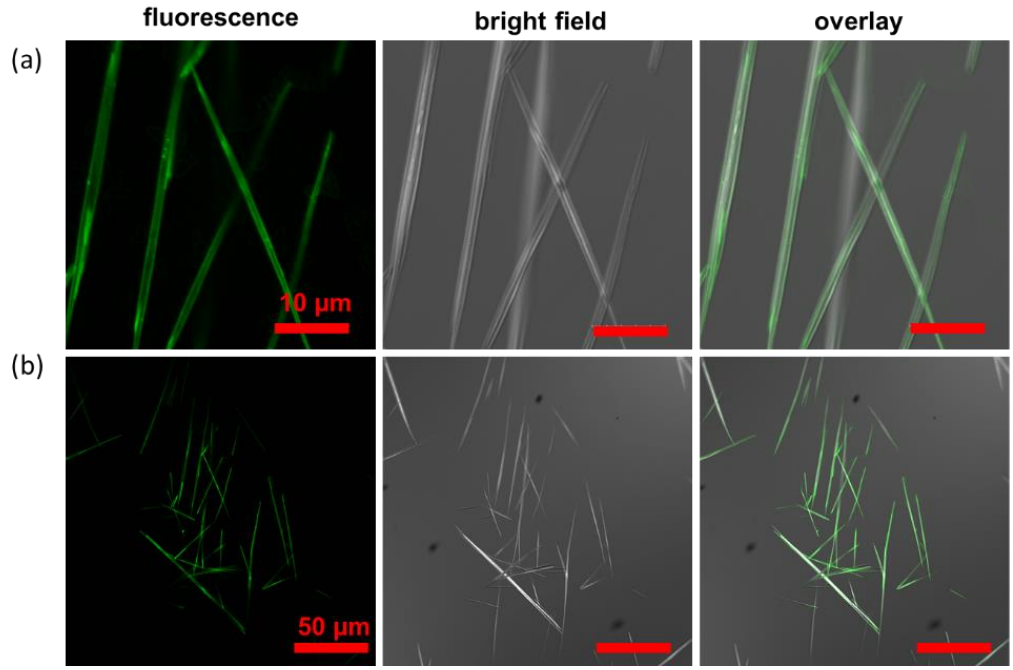


Figure S7. Confocal laser scanning micrographs showing the fluorescence (left), bright field (center), and overlay (right) images of FAOx-on-BioHOF-1 at two different magnifications.

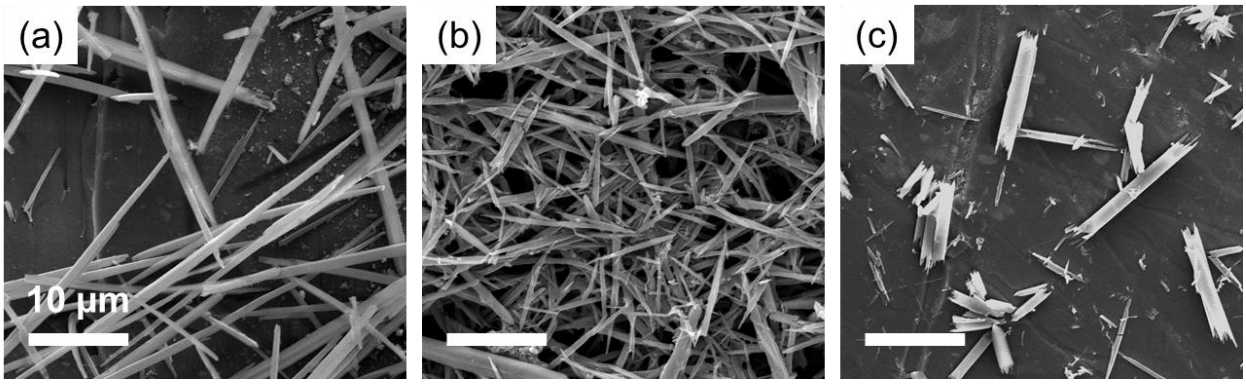


Figure S8. Scanning electron microscopy micrographs of (a) BioHOF-1, (b) FCAT@BioHOF-1, and (c) FAOx@BioHOF-1.

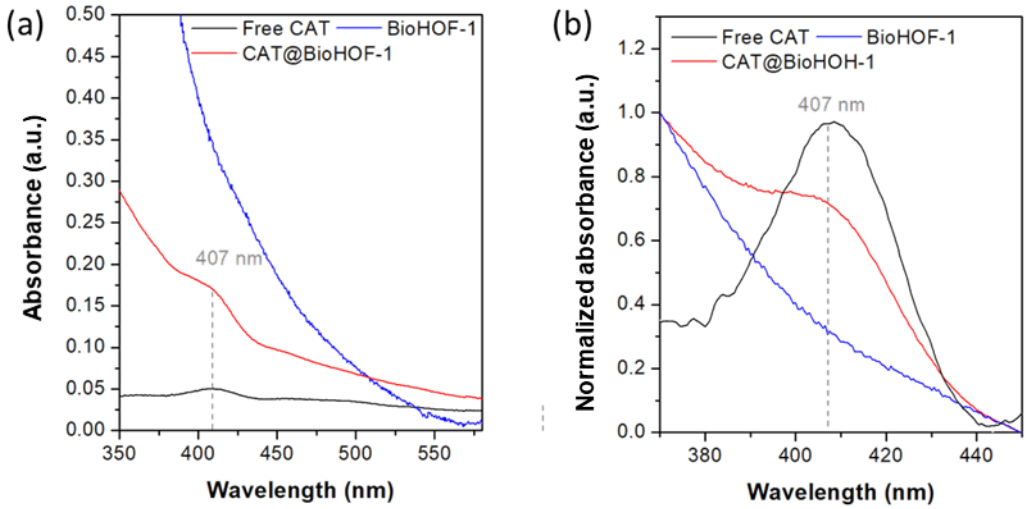


Figure S9. (a) Raw and (b) normalized solid-state UV–visible spectra for catalase (CAT) (black), CAT@BioHOF-1 (red), and BioHOF-1 (blue) samples.

## S4. Fluorescein adsorption

We assessed the porosity of BioHOF-1 in solution via fluorescein adsorption and also assessed ZIF-8, MAF-7 and ZIF-90, for comparison, under the same conditions. We posit that for applications, such as biocatalysis, the solution porosity of the HOF-biocomposite is practically important.

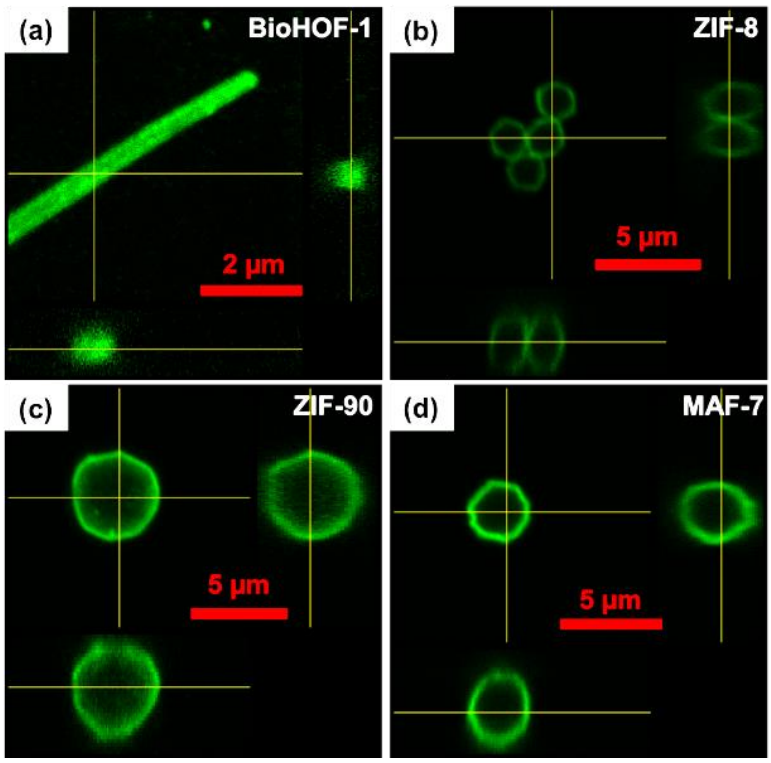


Figure S10. Ortho view of Z-stack fluorescence CLSM images of fluorescein/BioHOF-1 (a), fluorescein/ZIF-8 (b), fluorescein/ZIF-90 (c), and fluorescein/MAF-7 (d). The contact time for fluorescein and BioHOF-1 was 4 hours, while 24 hours for ZIFs.

Close inspection of CLSM experiments (Figure S10) show that BioHOF-1 adsorbs fluorescein homogeneously throughout its framework (a), while for the ZIF-based materials the dye does not adsorb within the pore network but remains on the crystal surface (b-d). This can be rationalized as the pore apertures of the ZIFs are <5 Å. This experiment highlights one advantage of the larger pore apertures of BioHOF-1

Furthermore, we assessed the porosity of BioHOF-1 to fluorescein after exposure to pH 5, pH 10 and 70˚C for 30 min, respectively. In each case, CLSM data (Figure S11) show that the fluorescent dye adsorbs into the framework pores.

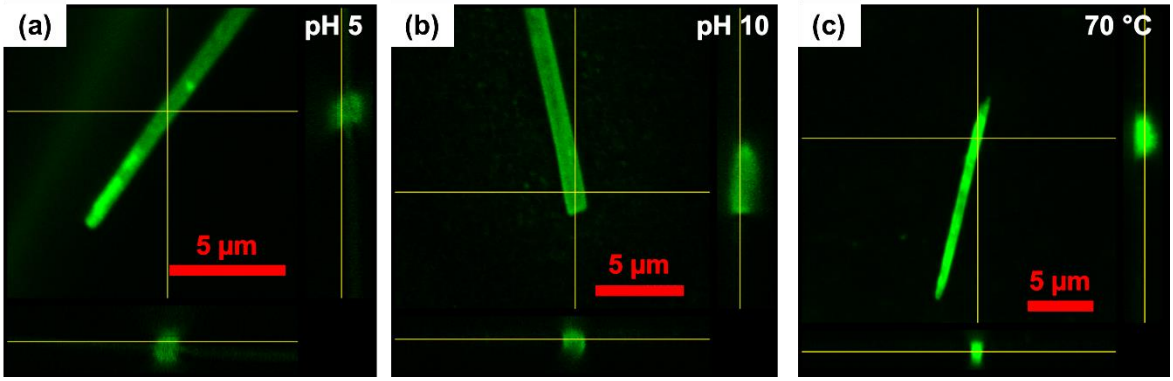


Figure S11. Ortho view of Z-stack fluorescence CLSM images of fluorescein/BioHOF-1 after different treatment: (a) 30 min in 0.1 M citric-sodium citrate buffer (pH 5); (b) 30 min in 0.1 M glycine-HCl buffer (pH 10); and 30 min of thermal treatment (70 °C).

# S5. Stability testing

### S5.1 Phosphate Buffer Saline media at pH=7.4

**$^1$H NMR Spectroscopy Data**

We exposed 0.5 mg BioHOF-1 to 1 mL of a standard PBS solution (1x, prepared in deuterated water, pH=7.4) for one hour at room temperature. After one hour, the powder was collected via centrifugation and the supernatant was directly measured via $^1$H NMR (200 MHz) spectroscopy. By comparing the signal of amidinium in the supernatant (Figure S12, red line) to the amount required for the preparation of 0.5 mg of BioHOF-1 (Figure S12, black line) we estimated that less than 4% of the amidinium was released into the PBS media.

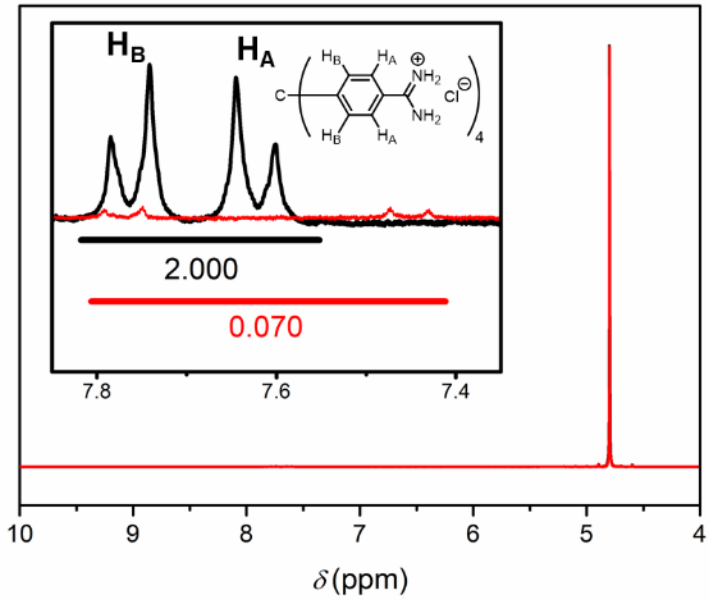


Figure S12. $^1$H NMR spectrum of tetrakis(4-amidiniumphenyl)methane (0.25 mg mL$^{-1}$)(black) and the BioHOF-1 supernatant (red) after letting BioHOF-1 soak in PBS saline (1 x, $D_2O$, 1 mL) for 1 h. Spectra were referenced to $D_2O$ ($\delta$ = 4.80 ppm) (512 scans).

The same experimental conditions were recently used to examine the stability of 0.5 mg of ZIF-8 in 1 mL of a standard PBS solution (1x, pH=7.4) by M. de J. Velasquez-Hernandez et al.[4] The authors attributed the dissolution to the affinity between the phosphate anions in the buffer solution and $Zn^{2+}$ ions in ZIF-8. Based on these data, we can confirm that BioHOF-1 is stable in physiological conditions that compromize the structural integrity of ZIF-8.

### S5.2 Buffer solution in the 4≤pH≤7.4 range

**Raman Spectroscopy Data**

We also employed Raman microscopy to further ascertain the stability of BioHOF-1 and ZIF-8 at different pH values (including 1 x PBS at pH 7.4). Raman spectra were recorded on a Thermo Fisher DXR2 Microscope (50xLWD Olympus objective ) equipped with a 785 nm laser operating at 35 mW. Briefly, we drop-cast 100 µL of a 10 mg $ml^{-1}$ BioHOF-1 dispersion in deionized water on Si wafers (100) (1.5 × 1.5 cm). The identical procedure was used to deposit ZIF-8 powders on Si wafers. The drop-cast samples were dried overnight at room temperature. Then, we exposed the BioHOF-1 and ZIF-8 samples to 2 mL of different buffer solutions such as:

- pH 7.4: PBS (1x);
- pH 6: PBS (1x);
- pH 5: PBS (1x);
- pH 4: sodium acetate buffer (0.1 M).

After immersion, we monitored the integrated intensity of characteristic Raman bands of the two materials (Figure S13, a, c, e, and g = BioHOF-1, b, d, f, and h = ZIF-8) for 30 minutes. Based on the collected data, we confirm significant degradation of ZIF-8 occurs within 30 min. However, BioHOF-1 is stable under the same conditions. We also show (Figure S14) the integrated intensity of the Raman band at 790 $cm^{-1}$ of BioHOF-1 and 1458 $cm^{-1}$ of ZIF-8 measured during 30 minutes of exposure to the pH 4-7.4 (100% corresponds to the integrated intensity of the analyzed Raman band 30 s after the exposure to the solution).

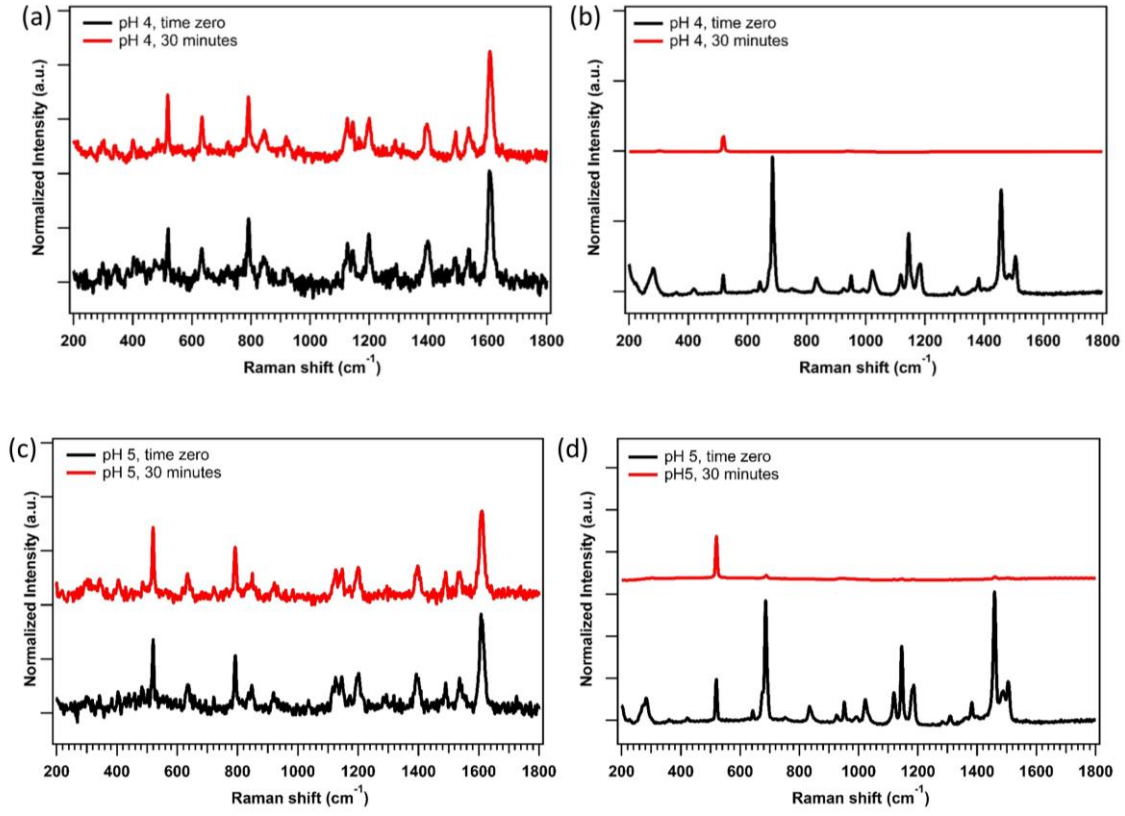

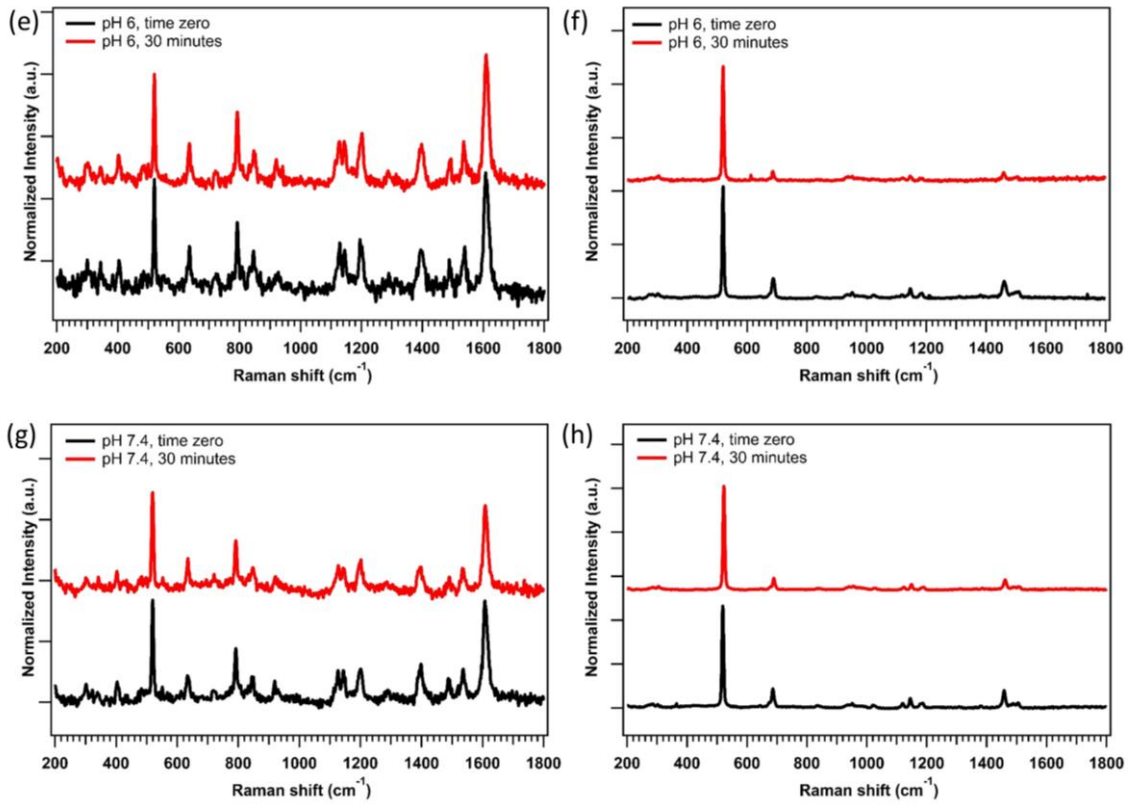


Figure S13. Raman spectra showing stability of BioHOF-1 (a,c,e,g) and ZIF-8(b,d,f,h) from pH 4 to pH 7.4.

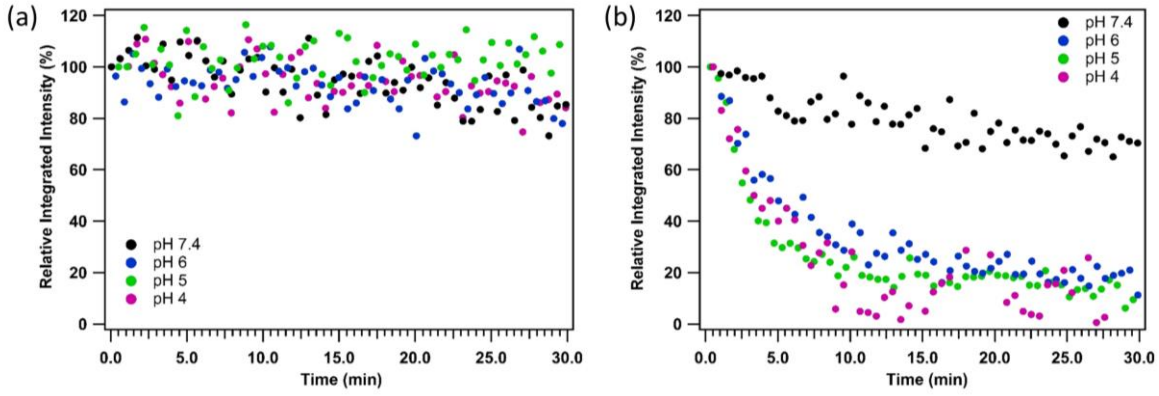


Figure S14. Relative integrated intensity of the Raman band at 790 $cm^{-1}$ of BioHOF-1 (a) and 1458 $cm^{-1}$ of ZIF-8 (b) measured during 30 minutes of exposure to pH 4-7.4 solution. 100% corresponds to the integrated intensity of the analyzed Raman band 30 s after the exposure to the solution.

**X-ray Diffraction (XRD) data**

A long term stability test (24 h exposure) was performed by exposing the previously described drop-cast films of BioHOF-1 and ZIF-8 to:

- pH 7.4: PBS (1x);
- pH 6: PBS (1x);
- pH 5: PBS (1x);
- pH 4: sodium acetate buffer (0.1 M).

Based on the XRD patterns we can confirm the results in previous reports[4, 5] that ZIF-8 degrades in PBS solutions and in acidic conditions. Conversely, BioHOF-1 is stable under identical conditions Figure S15.

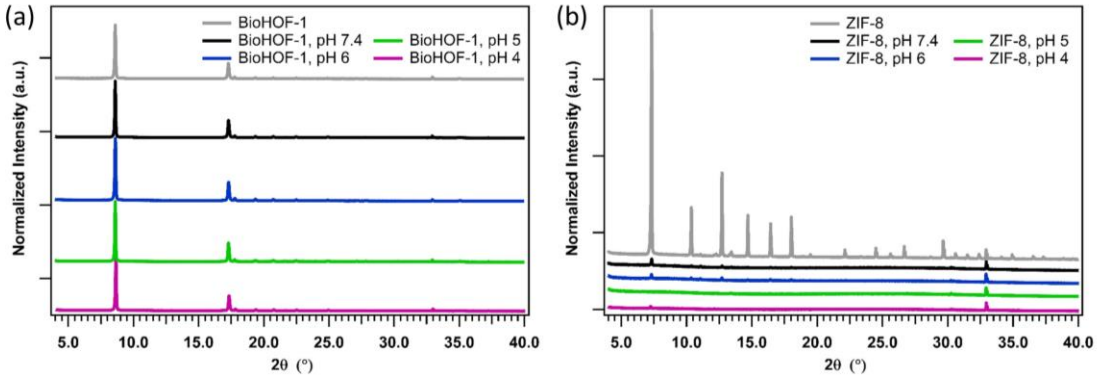


Figure S15. XRD patterns showing the stability of BioHOF-1 (a) and ZIF-8 (b) from pH 4-7.4. The intensity of the patterns are normalized to the intensity of the Si (002) substrate diffraction peak (2θ=32.9°).

**FTIR Spectroscopy**

Fourier Transformed Infrared (FTIR) data reveals differences between the drop-cast BioHOF-1 crystals and its constituent building blocks (Figure S16). For the tetracarboxylate ligand, the shift in the ketone νC=O = 1701 $cm^{-1}$ and the carboxylate νC-O =1253 $cm^{-1}$ suggest a restriction of movement in the functional group associated with hydrogen bonding. Likewise, for the amidinium ligand, the shift in νC=N = 1691 $cm^{-1}$ (imine) and a shift in the broad band at 3000-3700 $cm^{-1}$ (assigned partly to $\nu NH_2$ in the amidinium), also supports the generation of a rigid structure. The invariance of the IR spectra as a function of pH suggests that degradation of the HOF structure is limited.

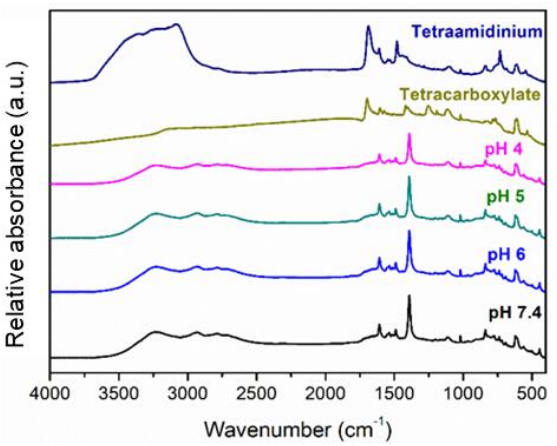


Figure S16. FTIR (transmission mode) of BioHOF-1 at varying pH (from 4-7.4), as well as the non-coordinated building blocks after exposure to buffered solutions for 24-hour. (32 scans).

**UV-Vis Spectroscopy**

We collected UV-vis spectroscopic data on the supernatants of BioHOF-1 exposed to the pH range 4-7.4. Compared to the signal obtained by dissolving the amount of building blocks needed for the preparation of 0.5 mg of BioHOF-1 (Figure S17), in the collected supernatants we observed a negligible absorbance of the BioHOF-1 precursors. These data suggest that negligible free ligand is leaching from BioHOF-1 after exposure to the different media.

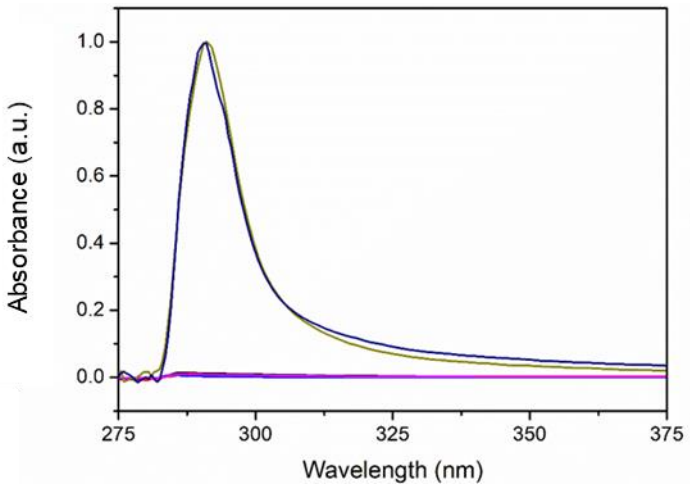


Figure S17. UV-Vis specta of the supernatant after suspension in buffer at pH 4 (black), pH 5 (red), pH 6 (blue), and pH 7.4 (pink). UV-Vis spectra of the identical building block ligand at pH 4 (yellow) and pH 7.4 (navy).

### S5.3 Acqueus solution, pH=14

We also investigated the stability of BiOHOF-1 at pH 14 (NaOH 1M solution) using Raman spectroscopy and XRD. BioHOF-1 and ZIF-8 were tested under these extreme basic conditions and ZIF-8 showed superior structural stability. Even though, XRD and Raman experiments show that BioHOF-1 is not stable at pH 14 we do not believe this is likely to be a problem for biological applications, as these do not occur under these highly basic conditions. As shown in the previous section, BioHOF-1 shows far better stability in biologically-relevant conditions than ZIF materials.

**Raman Spectroscopy, pH 14 stability**

Raman spectra were recorded on a Thermo Fisher DXR2 Microscope (50xLWD Olympus objective) equipped with a 785 nm laser operating at 35 mW. Briefly, we drop-cast 100 µL of a 10 mg $ml^{-1}$ BioHOF-1 dispersion in deionized water on Si wafers (100) (1.5 x 1.5 cm). The drop-cast samples were dried overnight at room temperature. We exposed the BioHOF-1 film to 2 mL of 1M NaOH solution and we monitored for 30 minutes the integrated intensity of the Raman band at 790 $cm^{-1}$ associated to the ring vibration of para-disubstituted benzene rings[6] of BioHOF-1. For comparison, we performed the same experiment with drop-cast ZIF-8 using the same protocol and basic conditions. In the case of ZIF-8, we

monitored the integrated intensity of the Raman band at 1458 $cm^{-1}$ assigned to methyl bending.[7, 8] In Figure S18a we plot the relative integrated intensity of the Raman band at 790 $cm^{-1}$ of BioHOF-1 and at 1458 $cm^{-1}$ of ZIF-8 measured during 30 minutes of exposure to the pH 14 NaOH solution. 100% corresponds to the integrated intensity of the analyzed Raman band 30 s after the exposure to the NaOH solution. For ZIF-8, the integrated intensity of the selected band does not change over time. The same is valid for all the other vibrational bands of the ZIF-8 spectrum. Thus, we can conclude that ZIF-8 is stable at pH=14. For BioHOF-1 the intensity rapidly decreases, dropping to a 20% of the starting value in only 5 minutes. This demonstrates that BioHOF-1 rapidly degrades at pH=14.

**XRD Data, pH 14 stability**

To assess the long-term stability, we measured the XRD pattern of the drop-cast films after 24-hour exposure to 1M NaOH (pH=14) and compared these data with the patterns of the untreated samples (Figure S18 b and c). Based on the missing diffraction peaks, we can conclude that BioHOF-1 is completely dissolved. Conversely, the diffraction pattern of ZIF-8 shows only a decrease of the diffraction peaks intensity, confirming the stability of ZIF-8 sample in the extreme basic conditions.

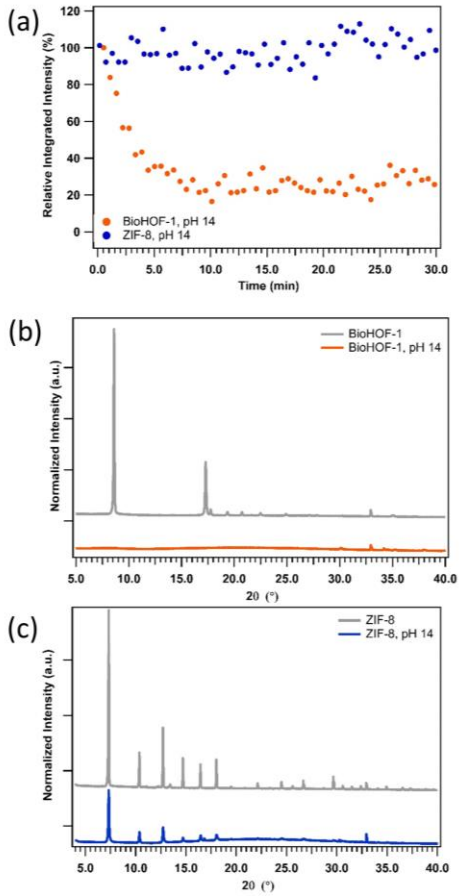


Figure S18. (a) Relative integrated intensity of the Raman band at 790 $cm^{-1}$ of BioHOF-1 and at 1458 $cm^{-1}$ of ZIF-8 measured during 30 minutes of exposure to the pH 14 NaOH solution. 100% corresponds to the integrated intensity of the analyzed Raman band 30 s after the exposure to the NaOH solution. XRD

patterns of BioHOF-1 (b) and ZIF-8 (c) drop-cast films as-prepared (gray lines) and after 24-hour exposure to 1 M NaOH solution (pH=14). The intensity of the patterns are normalized to the intensity of the Si (002) substrate diffraction peak ($2\theta$=32.9°).

## S6. Screening of washing procedures

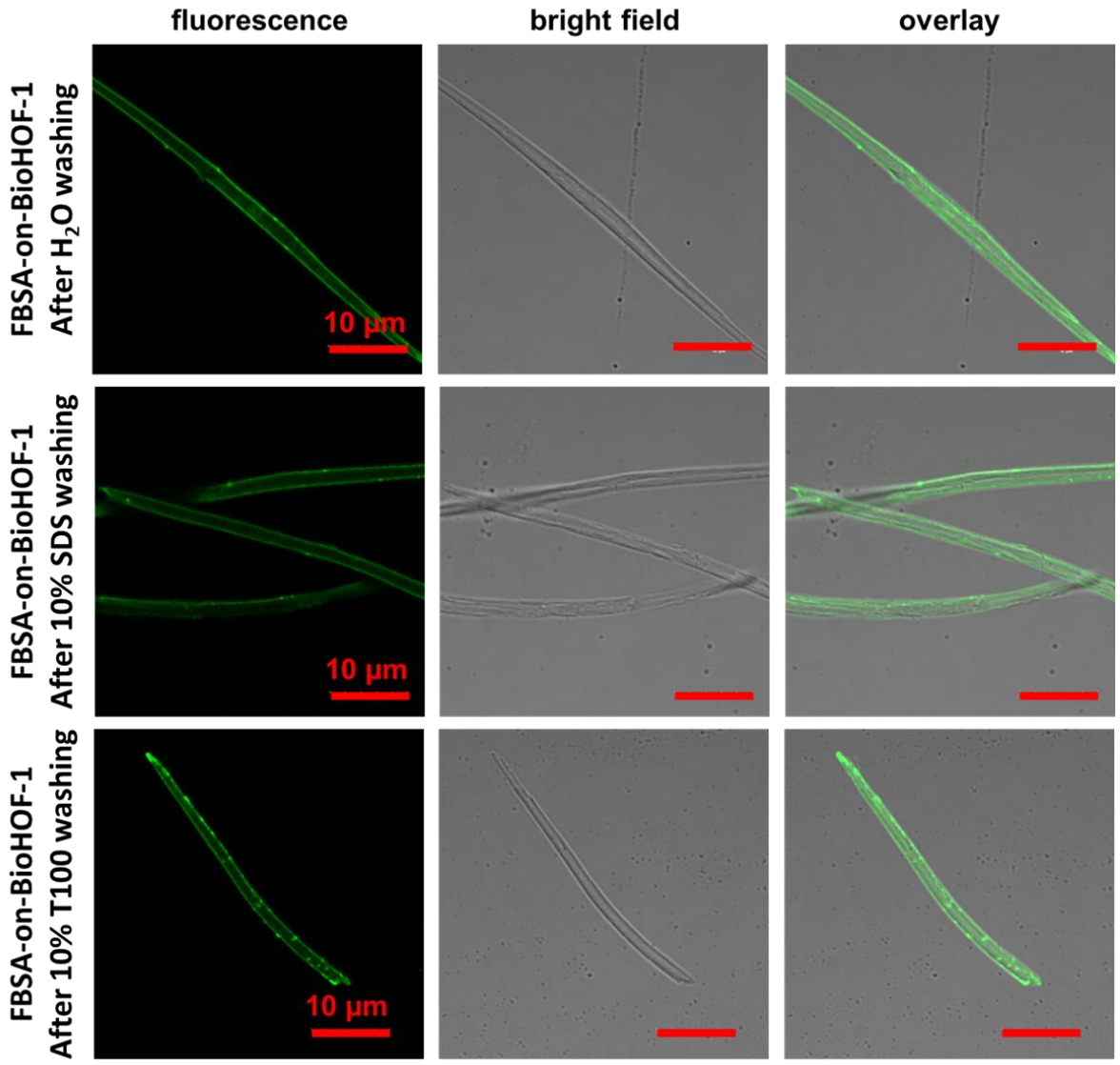


Figure S19. CLSM micrographs showing the fluorescence, bright field, and overlay images of FBSA-on-BioHOF-1 after $H_2O$ (a), 10% SDS (b; SDS = sodium dodecyl sulfate; w/w; in $H_2O$), and 10% T100 (c; T100 = Triton$^{TM}$ X100; w/w; in $H_2O$) washing.

Fluorescein-tagged BSA (FBSA) was chosen as a model protein for washing procedure screening. FBSA was synthesized using analogous method as FCAT and FAOx.

Rigorous washing procedures (e.g. 10% w/w aq sodium dodecyl sulfate (SDS)) could not effectively remove the surface-adsorbed BioHOF-1 (Figures S19), and thus, to be consistent, all as-synthesized biocomposites were only washed with water to remove the loosely adsorbed protein on the BioHOF-1 surface.

## S7. Catalytic performance of FCAT and the FCAT@BioHOF-1 composite

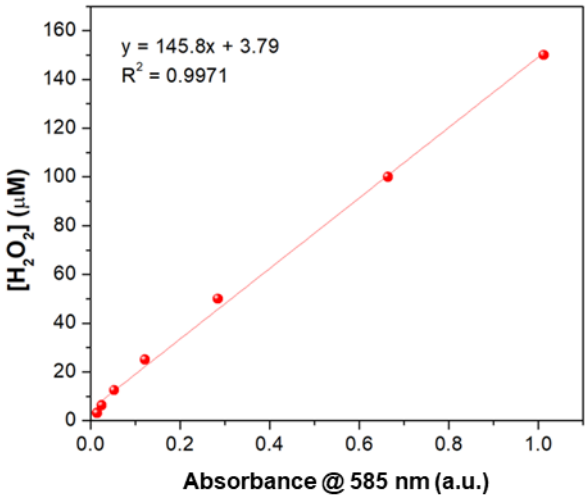


Figure S20. The calibration curve of the FOX (Ferrous Oxidation in Xylenol orange) assay. Briefly, $H_2O_2$ standard solutions (50 µL) at various concentrations were mixed with the FOX reagent (composed of 250 µM ammonium ferrous sulfate, 100 µM xylenol orange, 100 mM sorbitol in 25 mM $H_2SO_4$; 950 µL) and incubated for 30 min at room temperature before reading absorbance at 585 nm. The concentration of $H_2O_2$ was calibrated using an extinction coefficient of 39.4 $M^{-1}$ $cm^{-1}$ at 240 nm.

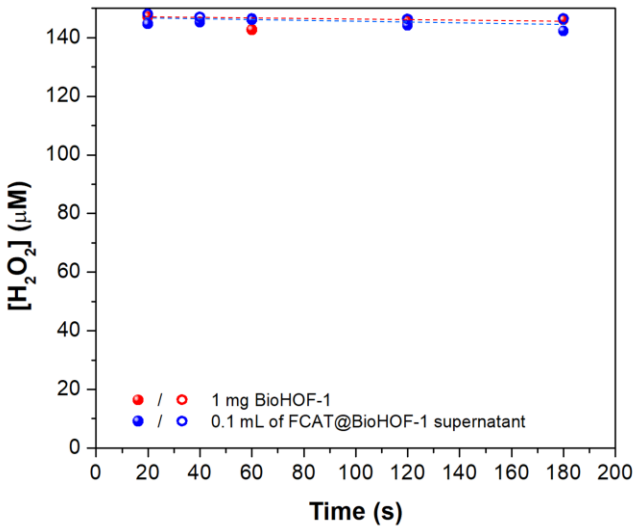


Figure S21. Catalytic activity of BioHOF-1 (red) and supernatant of FCAT@BioHOF-1 (blue). The assay was performed in phosphate buffer (pH 8, 100 mM) with BioHOF-1 material (0.1 mg) or FCAT@BioHOF-1 supernatant (0.1 mL) (FCAT@BioHOF-1 was stored in $H_2O$, 1.5 mL). The $H_2O_2$ concentration was 0.15 mM. Individual results for duplicate experiments are shown as open and closed circles.

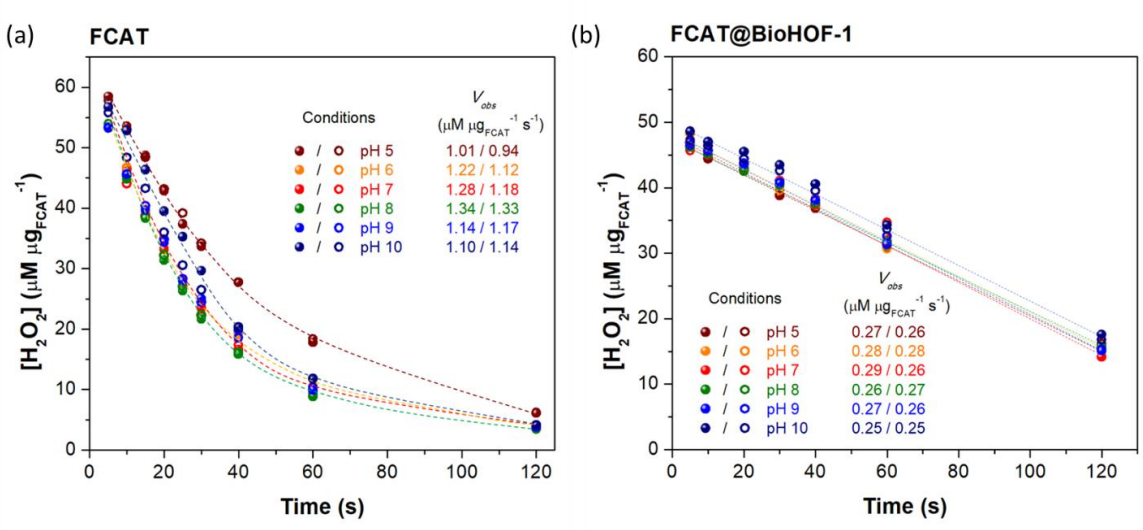


Figure S22. Biological activity of (a) free FCAT and (b) FCAT@BioHOF-1 composites in different pH conditions. The enzymatic assays were performed in citrate buffer (pH 5, 0.1 M), phosphate buffer (pH 6-8, 0.1 M), or glycine-HCl buffer (pH 9-10, 0.1 M) with $H_2O_2$ (0.15 mM). The total volume of the reaction mixture was fixed to 1 mL. The values of reaction rate ($V_{obs}$) is summarized in the inset of the figures. The FCAT dosage in the assay for FCAT and FCAT@BioHOF-1 were 2.6 and 2.9 μg (based on FCAT, determined by ICP-MS), respectively. Individual results for duplicate experiments are shown as open and closed circles.

The optimal operational pH for FCAT is determined to be pH 8 with $V_{obs}$ as *ca.* 1.34 μM $μg_{FCAT}^{-1}$ $s^{-1}$. The optimal operational pH for FCAT@BioHOF-1 is determined to be pH 7 to 8, with $V_{obs}$ as *ca.* 0.28 μM $μg_{FCAT}^{-1}$ $s^{-1}$. The relative activity (%) shown in Figure 2 was calculated by comparing the $V_{obs}$ for the catalyst after different treatment to the $V_{obs}$ of corresponding catalyst determined under optimal condition (pH 8, room temperature).

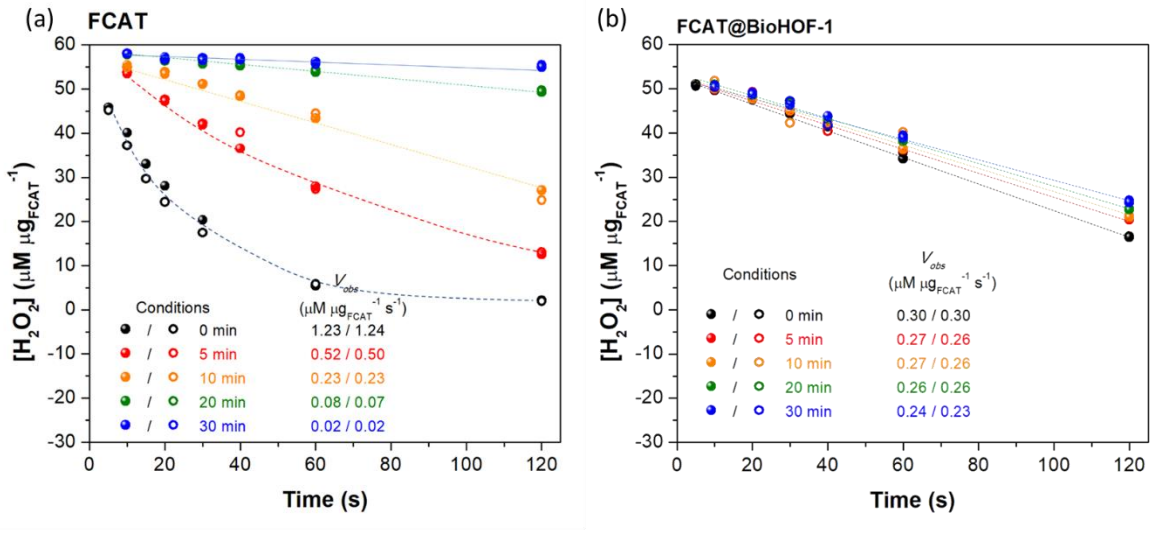


Figure S23. Biological activity of (a) free FCAT and (b) FCAT@BioHOF-1 after treatment in water for 0-30 min at 60 °C. The enzymatic assays were performed in phosphate buffer (pH 8, 0.1 M) with $H_2O_2$ (0.15 mM). The total volume of the reaction mixture was fixed to 1 mL. $V_{obs}$ is summarized in the inset of the figures. The FCAT dosage in the assay for FCAT and FCAT@BioHOF-1 were 2.6 and 2.9 μg (based on FCAT, determined by ICP-MS), respectively. Individual results for duplicate experiments are shown as open and closed circles.

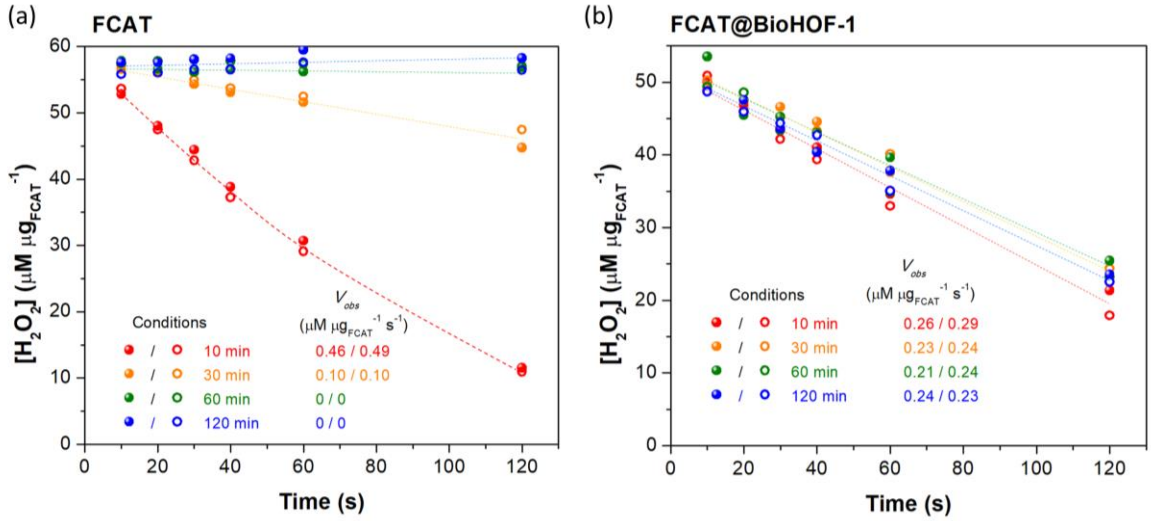


Figure 24. Biological activity of (a) free FCAT and (b) FCAT@BioHOF-1 after proteolytic agent treatment (2 mg $mL^{-1}$ trypsin in 0.1 M pH 8 phosphate buffer for 10-120 min). The enzymatic assays were performed in phosphate buffer (pH 8, 0.1 M) with $H_2O_2$ (0.15 mM). The total volume of the reaction mixture was fixed to 1 mL. $V_{obs}$ is summarized in the inset of the figures. The FCAT dosage in the assay for FCAT and FCAT@BioHOF-1 were 2.6 and 2.9 μg (based on FCAT, determined by ICP-MS), respectively. Individual results for duplicate experiments are shown as open and closed circles.

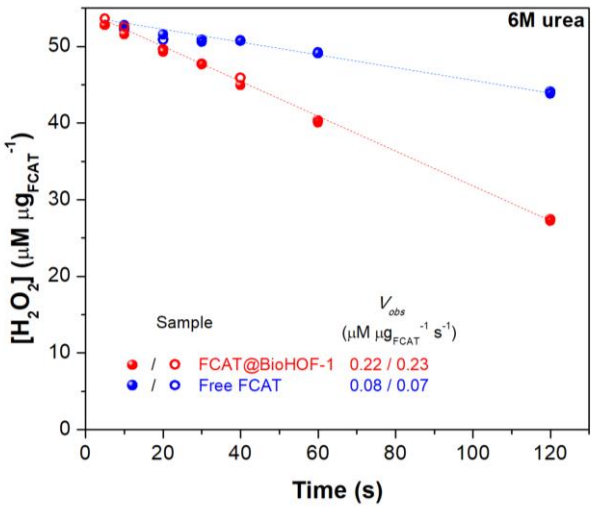


Figure S25. Biological activity of free FCAT and FCAT@BioHOF-1 after treatment with an unfolding agent (urea (6 M) in phosphate buffer (pH 8, 0.1 M) for 30 min). The enzymatic assays were performed in phosphate buffer (pH 8, 0.1 M) with $H_2O_2$ (0.15 mM). The total volume of the reaction mixture was fixed to 1 mL. The FCAT dosage in the assay for FCAT and FCAT@BioHOF-1 were 2.6 and 2.9 μg (based on FCAT, determined by ICP-MS), respectively. Individual results for duplicate experiments are shown as open and closed circles.

After urea (6 M) treatment for 30 min, FCAT and FCAT@BioHOF-1 retained *ca.* 6 % and 75 % of their original activity, respectively.

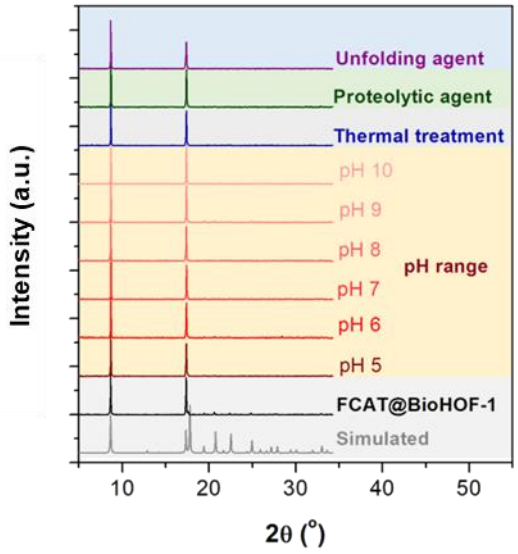


Figure S26. Experimental and simulated powder X-ray diffraction patterns of the as-synthesized FCAT@BioHOF-1 and composites after testing their stability.

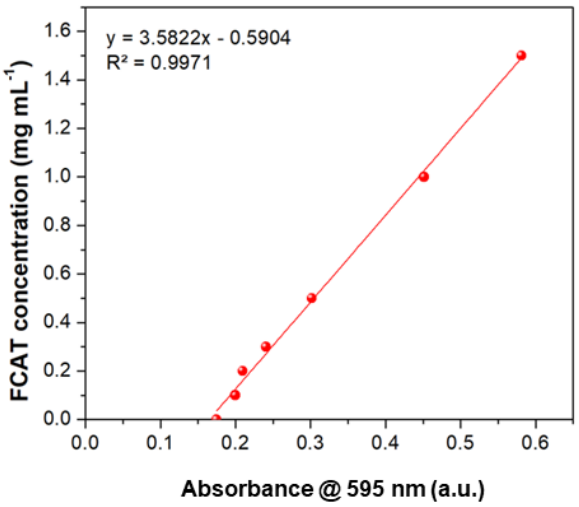


Figure S27. The calibration curve of FCAT concentration using the Bradford assay. The concentration of the FCAT stock solution was determined by ICP-MS (based on sulfur). This experiment was used to quantify the activity of the FCAT-on-BioHOF-1.

FCAT-on-BioHOF-1 was synthesized by mixing FCAT (0.2 mL of 2 mg $mL^{-1}$ FCAT stock solution) with the as-synthesized BioHOF-1 (5 mg) in $H_2O$ at room temperature for 1 h. Thereafter, the solid was recovered by centrifugation, and washed with $H_2O$ (3 times) to remove excess FCAT. All supernatants were collected. The concentration of FCAT in the supernatant was determined by Bradford assay. The amount of FCAT adsorbed on FCAT-on-BioHOF-1 was calculated by the difference between the FCAT used in the synthesis and that in the collected supernatant.

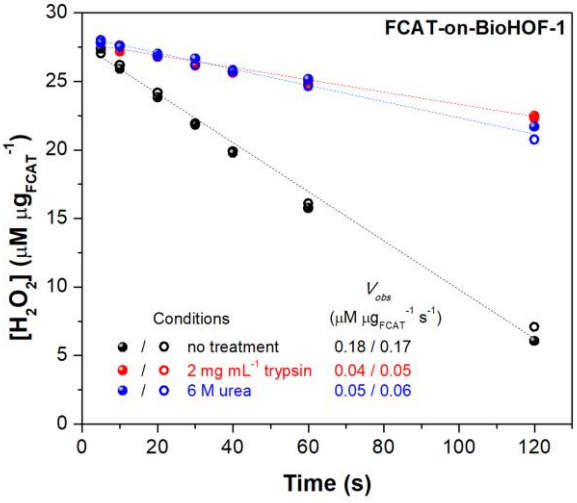


Figure S28. Biological activity of FCAT-on-BioHOF-1 before and after unfolding agent treatment (urea (6 M) in phosphate buffer (pH 8, 0.1 M) for 30 min) or proteolytic agent treatment (trypsin (2 mg $mL^{-1}$) in phosphate buffer (pH 8, 0.1 M) for 30 min). The enzymatic assays were performed in phosphate buffer (pH 8, 0.1 M) with $H_2O_2$ (0.15 mM). The total volume of the reaction mixture was fixed to 1 mL. The FCAT dosage in the assay for FCAT-on-BioHOF-1 was 5 μg (calculated by Bradford assay (Figure S27)). Individual results for duplicate experiments are shown as open and closed circles.

After urea (6 M) treatment for 30 min, FCAT-on-BioHOF-1 retained *ca.* 27 % of its original activity. After trypsin treatment, *ca.* 28 % of its original activity was retained for FCAT-on-BioHOF-1 sample.

The $V_{obs}$ for FCAT-on-BioHOF-1 measured under pH 8 (RT) is determined to be *ca.* 0.18 μM $μg_{FCAT}^{-1}$ $s^{-1}$. The relative activity (%) was calculated by comparing the $V_{obs}$ for the catalyst after different treatment to the $V_{obs}$ of corresponding catalyst determined under optimal condition (pH 8, room temperature).

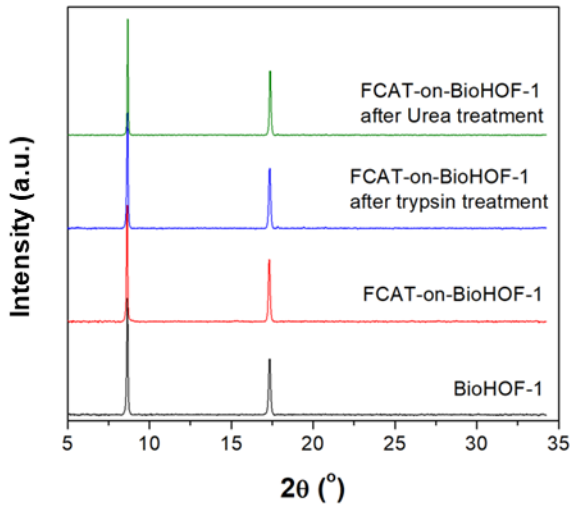


Figure S29. Experimental powder X-ray diffraction patterns of the as-synthesized FCAT-on-BioHOF-1 and composites before and after treatment with trypsin (blue) and Urea (green).

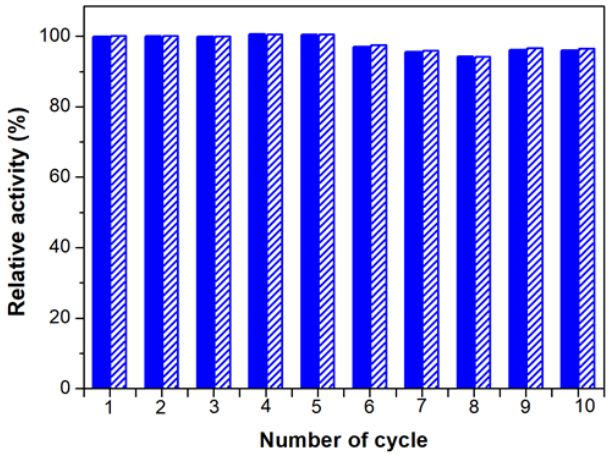


Figure S30. Cycling runs for the degradation of $H_2O_2$ (0.15 mM) in the presence of FCAT@BioHOF-1 (6 μg, based on FCAT) at room temperature. Individual results for duplicate experiments are shown as filled and shaded bars.

The enzymatic assays were performed in phosphate buffer (pH 8, 0.1 M) with $H_2O_2$ (0.15 mM). The total volume of the reaction mixture was fixed to 1 mL. The amount of residual $H_2O_2$ in the solution was checked 3 min after the addition of $H_2O_2$ in the reaction mixture. After each run, the sample was washed with $H_2O$ (0.5 mL) and centrifuged for 5 min. Thereafter, the supernatant was decanted and the FCAT@BioHOF-1 catalyst in the Eppendorf tube was subjected to next cycle run.

The turn over number (TON) was calculated to be 15000. TON = (mol of $H_2O_2$ over ten cycling experiments) / (mol of FCAT in FCAT@BioMOF-1); molecular weight of FCAT was estimated to be the same as CAT as 60 kDa.

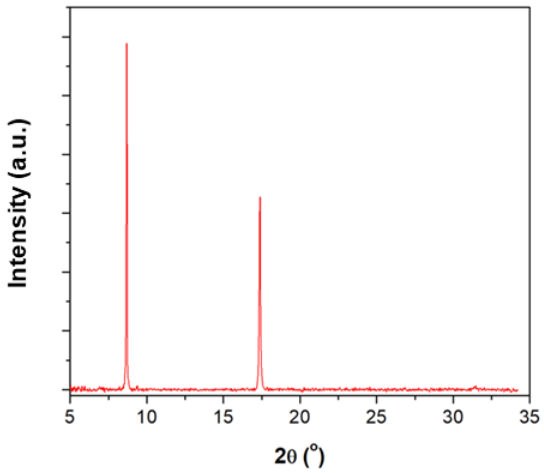


Figure S31. PXRD pattern for FCAT@HOF after recycling experiments.

## S8. Synthesis, characterization, and catalytic performance of FAOx/ZIF biocomposites

AOx catalyzes the oxidation of short aliphatic alcohols to formaldehyde with concomitant production of $H_2O_2$.[9]

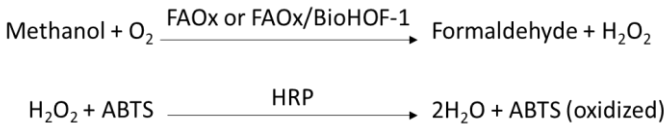


**Syntheses**

**Synthesis Method for FAOx@ZIF-8**

FAOx@ZIF-8 was synthesized in water with $Zn(OAc)_2 \cdot 2H_2O$ (40 mM), 2-methylimidazole (HmIM, 640 mM), and FAOx (0.33 mg $mL^{-1}$) at room temperature under static condition (without stirring) for 24 h. In a typical synthesis, 157.4 mg of HmIM was dissolved in 2.3 mL of $H_2O$. Thereafter 0.5 mL of FAOx solution (2 mg $mL^{-1}$) was introduced followed by the addition of $Zn(OAc)_2 \cdot 2H_2O$ solution (26.3 mg in 0.2 mL of $H_2O$). The total volume of the reaction mixture was 3 mL. The precipitate was recovered by centrifugation at 10,000 rpm for 5 min (SIGMA 1-14K) and then washed, sonicated, and centrifuged three times each in ultrapure water to remove loosely adsorbed FAOx.

**Synthesis Method for FAOx@ZIF-90**

FAOx@ZIF-90 was synthesized in water with $Zn(NO_3)_2 \cdot 6H_2O$ (40 mM), 2-imidazole carboxaldehyde (HICA, dissolved at elevated temperature in $H_2O$; 160 mM), and FAOx (0.33 mg $mL^{-1}$) at room temperature under static condition for 24 h. In a typical synthesis, 46 mg of HICA was dissolved in 2.3 mL of $H_2O$ at elevated temperature. After cooling to around 30 °C, 0.5 mL of FAOx solution (2 mg $mL^{-1}$) was introduced followed by the addition of $Zn(NO_3)_2 \cdot 6H_2O$ solution (35.7 mg in 0.2 mL of $H_2O$). The total volume of the reaction mixture was 3 mL. The precipitate was recovered by centrifugation at 10,000 rpm for 5 min (SIGMA 1-14K) and then washed, sonicated, and centrifuged three times each in ultrapure water to remove loosely adsorbed FAOx.

**Synthesis Method for FAOx@MAF-7**

FAOx@MAF-7 was synthesized in water with $Zn(NO_3)_2 \cdot 6H_2O$ (40 mM), 3-methyl-1,2,4-triazole (Hmtz, 160 mM), 10% $NH_3 \cdot H_2O$ (60 μL) and FAOx (0.33 mg $mL^{-1}$) at room temperature under stirring for 24 h. In a typical synthesis, 40 mg of Hmtz was dissolved in a mixture of 2.24 mL of $H_2O$ and 0.06 mL of 10% $NH_3 \cdot H_2O$. Thereafter, 0.5 mL of FAOx solution (2 mg $mL^{-1}$) was introduced followed by the addition of $Zn(NO_3)_2 \cdot 6H_2O$ solution (35.7 mg in 0.2 mL of $H_2O$). The total volume of the reaction mixture was 3 mL. The precipitate was recovered by centrifugation at 10,000 r.p.m. for 5 min (SIGMA 1-14K) and then washed, sonicated, and centrifuged three times each in ultrapure water to remove loosely adsorbed FAOx.

**Synthesis Method for the FAOx-on-ZIF materials**

FAOx-on-ZIFs were synthesized by mixing FAOx (0.2 mL of 2 mg $mL^{-1}$ FAOx stock solution) with the as-synthesized ZIF (5 mg; ZIF = ZIF-8, ZIF-90, or MAF-7) in $H_2O$ (1 mL) at room temperature for 1 h. Thereafter, the solid was recovered by centrifugation and washed with $H_2O$ (3 times) to remove the excess FAOx.

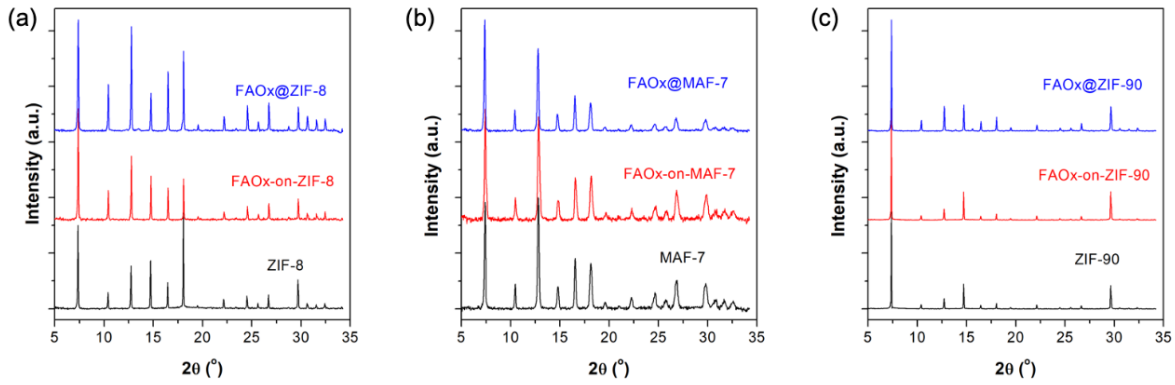


Figure S32. Experimental PXRD patterns for (a) ZIF-8, FAOx@ZIF-8, and FAOx-on-ZIF-8; (b) MAF-7, FAOx@MAF-7, and FAOx-on-MAF-7; and (c) ZIF-90, FAOx@ZIF-90, and FAOx-on-ZIF-90.

In each case, the crystallinity and topology of the ZIF were maintained (Figure S32). To quantify the amount of FAOx encapsulated within FAOx@ZIFs or adsorbed on FAOx-on-ZIFs, the biocomposites were dissolved in 1 mL of 0.1 M citric-sodium citrate buffer (pH 5). The fluorescence signal of FAOx in the dissolved samples were then measured by fluorescence spectroscopy (excited at 488 nm). The fluorescence maxima at 517 nm were recorded and compared to the calibration curve (Figure S33) to calculate the amount of FAOx.

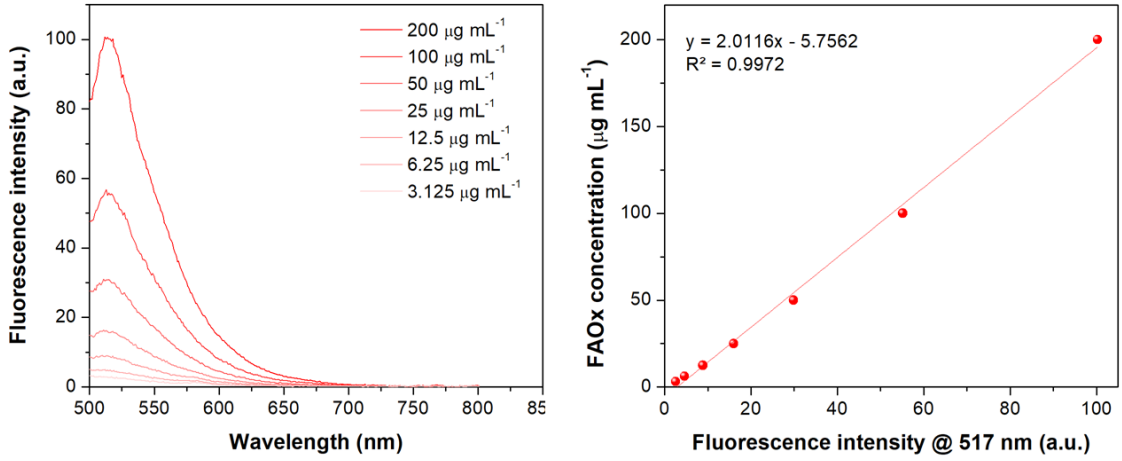


Figure S33. Calibration curve for FAOx in 0.1 M citric-sodium citrate buffer (pH 5) using the fluorescence spectroscopy technique. Samples were excited at 488 nm.

The spatial location of the enzyme in the ZIF-based biocomposites was examined using CLSM (Figures S34-S36).

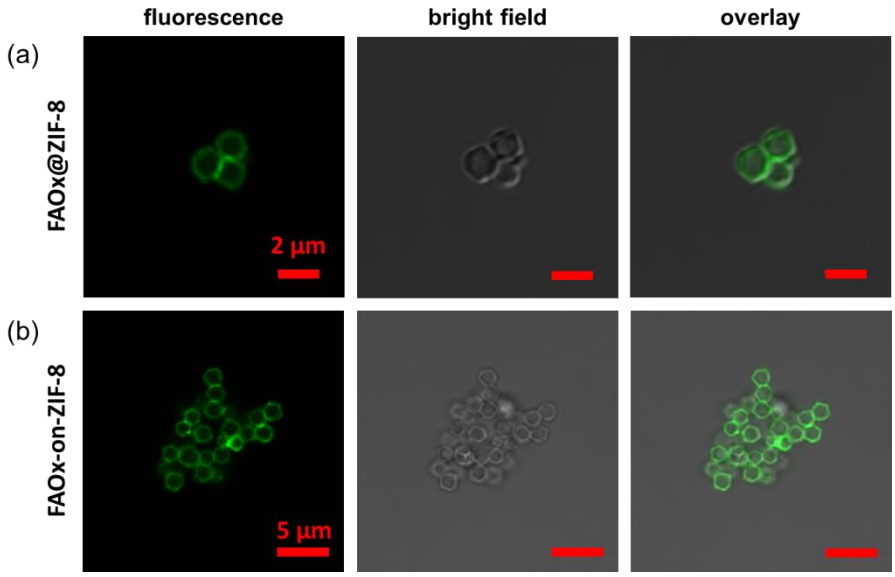


Figure S34. CLSM micrographs showing the fluorescence, bright field, and overlay images of (a) FAOx@ZIF-8 and (b) FAOx-on-ZIF-8.

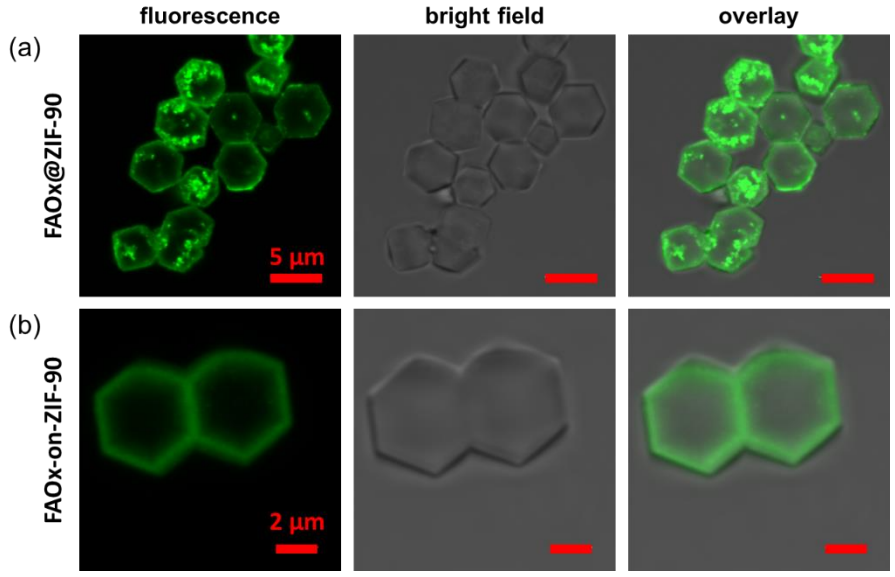


Figure S35. CLSM micrographs showing the fluorescence, bright field, and overlay images of (a) FAOx@ZIF-90 and (b) FAOx-on-ZIF-90.

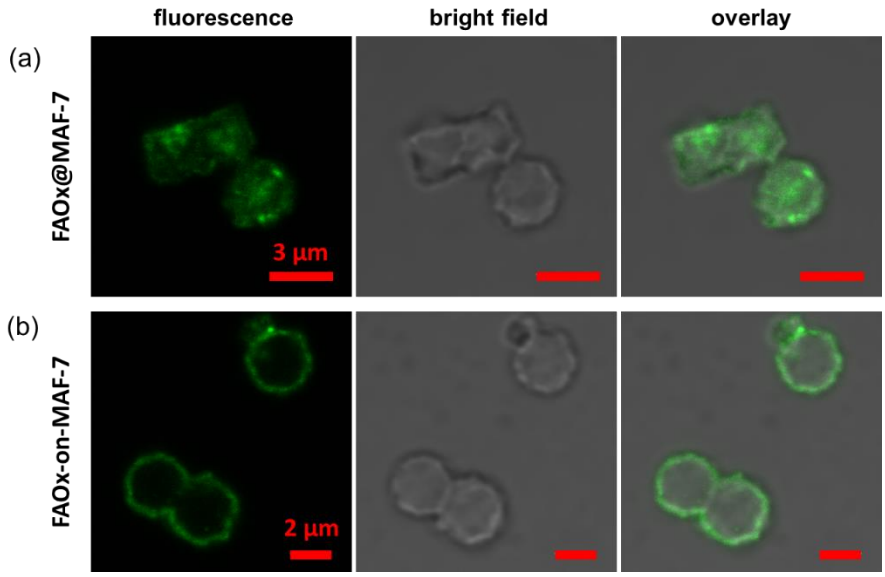


Figure S36. CLSM micrographs showing the fluorescence, bright field, and overlay images of (a) FAOx@MAF-7 and (b) FAOx-on-MAF-7.

Lastly, we performed activity assays for each of the composites (Figure S37). In all cases, the enzyme was found to be inactive.

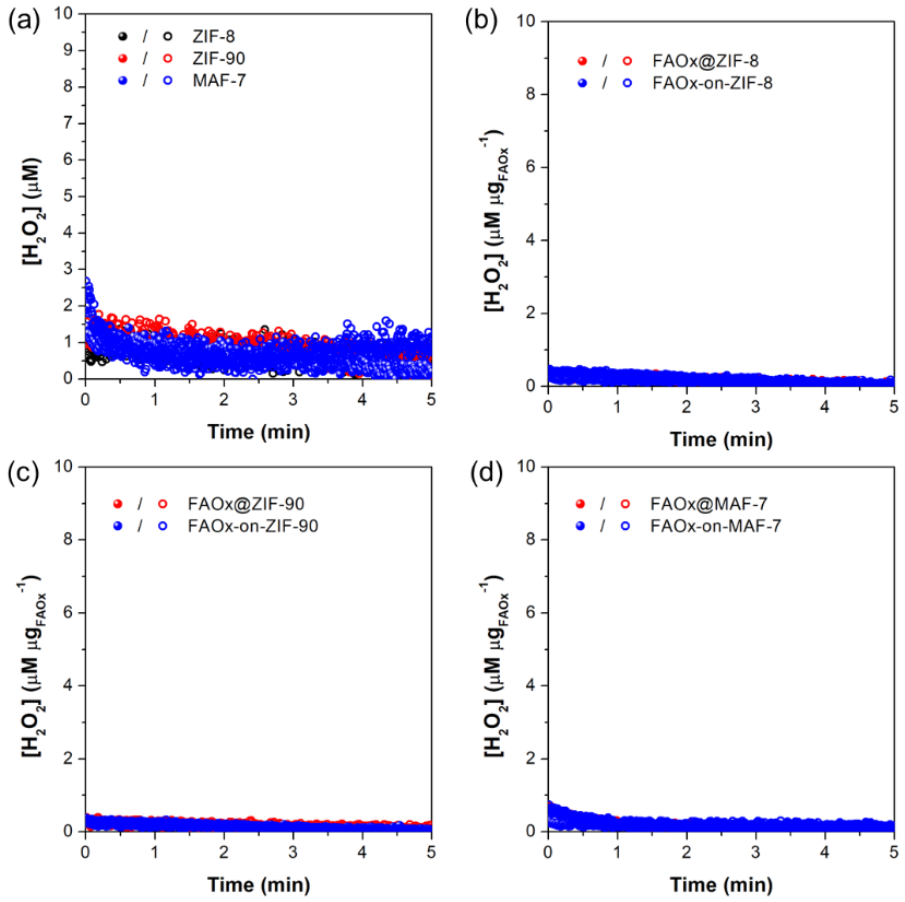


Figure S37. Catalytic activity of (a) ZIF-8, ZIF-90, and MAF-7; (b) FAOx@ZIF-8 and FAOx-on-ZIF-8; (c) FAOx@ZIF-90 and FAOx-on-ZIF-90; and (d) FAOx@MAF-7 and FAOx-on-MAF-7. The dosage of FAOx within the FAOx@ZIF or on the FAOx-on-ZIF samples in the assay test is 5 μg (based on the amount of FAOx, calculated by fluorescence spectroscopy). The amount of pure ZIF in the assay test is 1 mg. Individual results for duplicate experiments are shown as open and closed circles.

## S9. Catalytic performance of FAOx and FAOx@BioHOF-1 composite

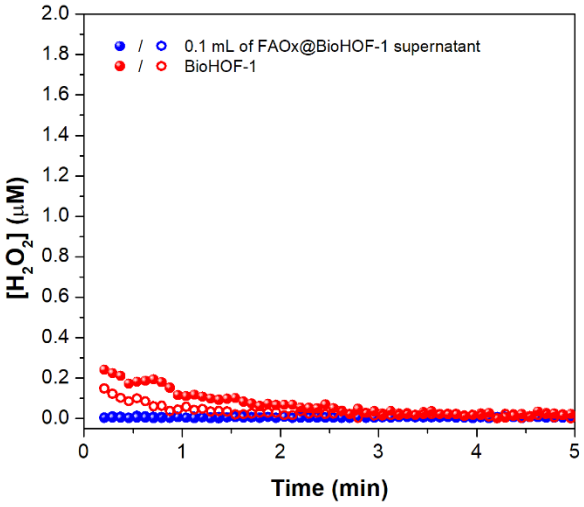


Figure S38. Catalytic activity of BioHOF-1 (red) and supernatant of FAOx@BioHOF-1 (blue). The assay was performed with 0.1 mg BioHOF-1 material or 0.1 mL of FAOx@BioHOF-1 supernatant (FAOx@BioHOF-1 were stored in 1.5 mL of $H_2O$). The initial drop of the BioHOF-1 measurement derived from the settlement of the BioHOF-1 particles. Individual results for duplicate experiments are shown as open and closed circles.

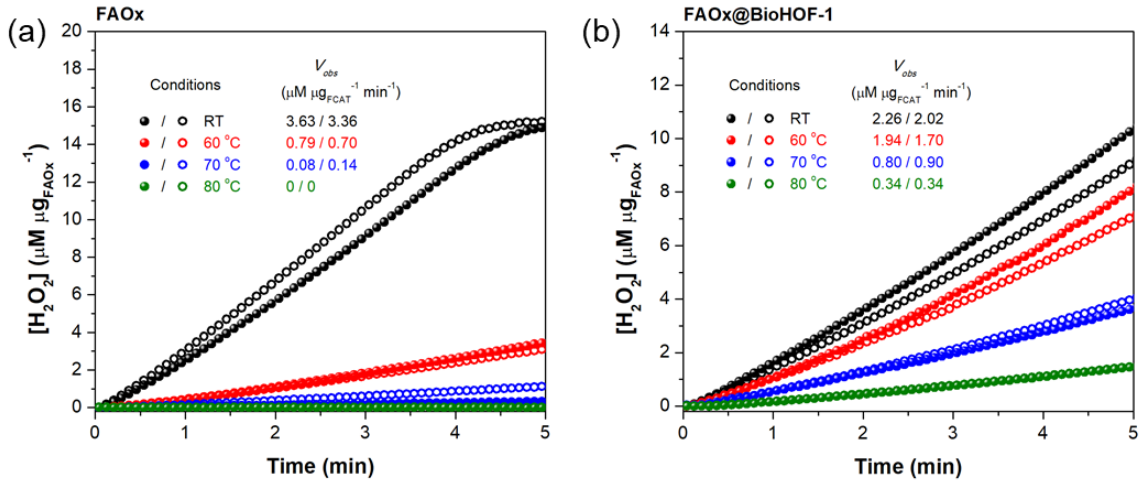


Figure S39. Catalytic activity of FAOx (a) and FAOx@BioHOF-1(b) after thermal treatment (60, 70, and 80 °C for 10 min) in water. After thermal treatment, the solution of FAOx or FAOx@BioHOF-1 was cooled down on ice before the measurement of their activity. The dosage of FAOx and FAOx@BioHOF-1 in the assay test is 9.4 and 11.2 μg (based on the amount of FAOx, calculated from ICP-MS), respectively. Individual results for duplicate experiments are shown as open and closed circles.

The $V_{obs}$ for FAOx and FAOx@BioHOF-1 measured under pH 7.5 (RT) is determined to be *ca.* 3.50 and 2.14 μM $\mu g_{FCAT}^{-1}$ $s^{-1}$, respectively. The values of relative activity in percentage were calculated by comparing the $V_{obs}$ for the catalyst after different treatment to the $V_{obs}$ of corresponding catalyst determined under optimal condition (pH 7.5, room temperature).

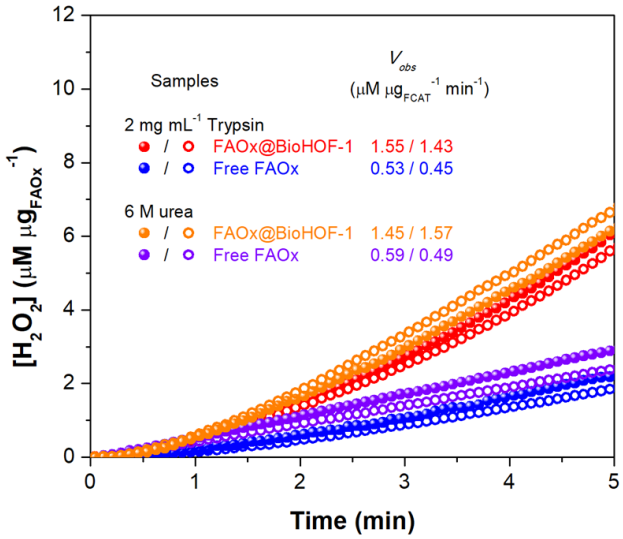


Figure S40. Catalytic activity of FAOx and FAOx@BioHOF-1 after proteolytic agent treatment (2 mg $mL^{-1}$ trypsin in pH 8 0.1 M phosphate buffer for 2 h) and after unfolding agent treatment (6 M urea in pH 8 0.1 M phosphate buffer for 30 min).. The dosage of FAOx and FAOx@BioHOF-1 in the assay test is 9.4 and 11.2 μg (based on the amount of FAOx, calculated by ICP-MS), respectively. Individual results for duplicate experiments are shown as open and closed circles.

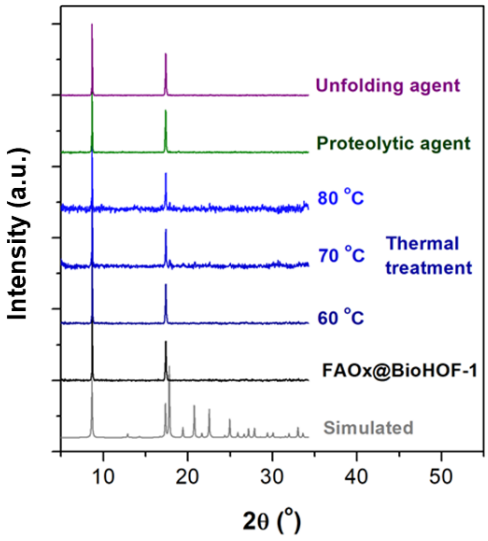


Figure S41. Experimental and simulated PXRD patterns of the as-synthesized FAOx@BioHOF-1 and composites after thermal (60, 70, or 80 °C for 10 min), proteolytic agent treatment (Trypsin (2 mg $mL^{-1}$) in phosphate buffer(pH 8, 0.1 M) or unfolding agent treatment (urea (6 M) in phosphate buffer (pH 8, 0.1 M)).

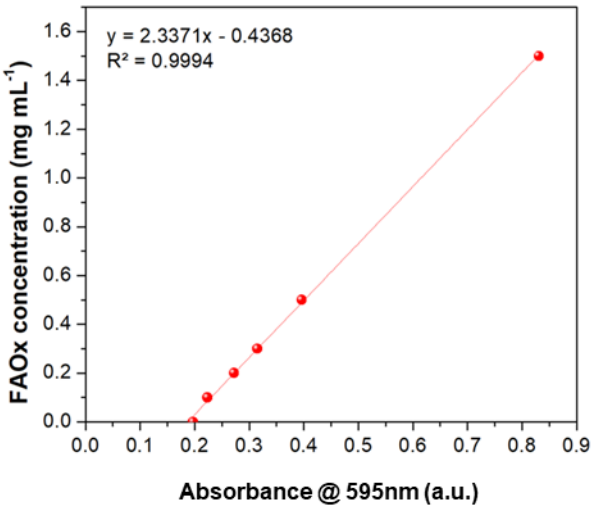


Figure S42. The calibration curve of FAOx concentration using the Bradford assay. The concentration of the FAOx stock solution was determined by ICP-MS (based on the sulfur element).

FAOx-on-BioHOF-1 was synthesized by mixing FAOx (0.2 mL of 2 mg $mL^{-1}$ FAOx stock solution) with the as-synthesized BioHOF-1 (5 mg) in $H_2O$ at room temperature for 1 h. Thereafter, the solid was recovered by centrifugation and washed with $H_2O$ (3 times) to remove the excess FAOx. All supernatants were collected. The concentration of FAOx in the supernatant was determined by the Bradford assay. The amount of FAOx adsorbed on FAOx-on-BioHOF-1 was calculated by the difference between the FAOx used in the synthesis and that in the collected supernatant.

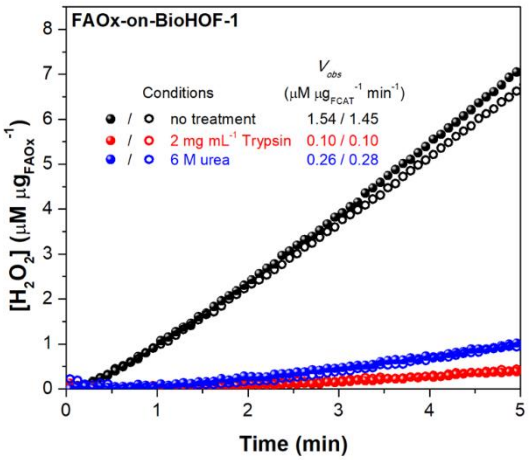


Figure S43. Catalytic activity of FAOx-on-BioHOF-1 before and after proteolytic agent treatment (trypsin (2 mg $mL^{-1}$) in phosphate buffer (pH 8, 0.1 M) for 2 h) or unfolding agent treatment (urea (6 M) in phosphate buffer (pH 8, 0.1 M) for 30 min). The dosage of FAOx-on-BioHOF-1 in the assay test is 10.5 μg (based on the amount of FAOx, calculated by Bradford assay (Figure S42)). After trypsin treatment, only *ca.* 7 % of the original activity was retained for FAOx-on-BioHOF-1 sample. After trypsin treatment, only 17 % of the original activity was retained for FAOx-on-BioHOF-1 sample. Individual results for duplicate experiments are shown as open and closed circles.

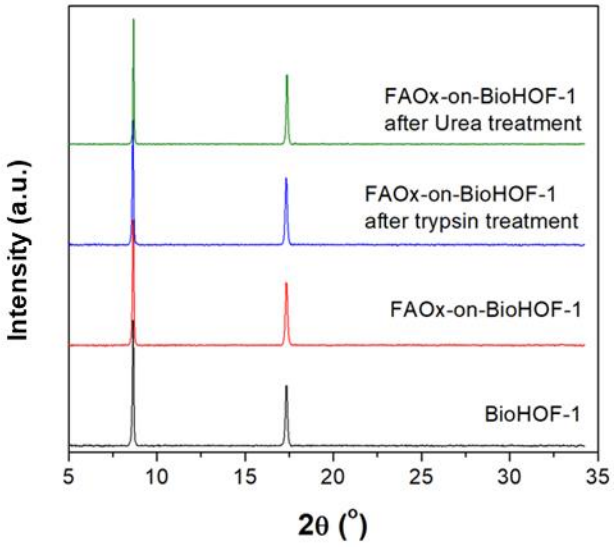


Figure S44. Experimental powder X-ray diffraction patterns of the as-synthesized FAOx-on-BioHOF-1 and the composites following stability testing.

## S10. Synchrotron Small Angle X-ray Scattering (SAXS) Experiments

Time-resolved SAXS experiments were performed using the stop-flow setup available at the SAXS beamline.[10, 11] The kinetics of the nucleation, growth and crystallization of the HOF particles were monitored in solution (time resolution 100 ms). In this study, BSA was used as a model biomolecule. The growth of BioHOF-1 particles was studied in presence and absence of the protein to investigate the role of BSA in their nucleation and growth.

Figure S45 reports the time evolution the integrated intensity of the (100) reflection at 6.1 $nm^{-1}$ (I (q=6.1 $nm^{-1}$)) and Porod Invariant (Q) for both the bare BioHOF-1 and for the BSA@BioHOF-1 composite material. Q is the integral parameter of an ensemble of particles proportional to their volume fraction and square to their electron denstity contrast.[12] In our case it is calculated in an limited *q* range i.e. 0.1 $nm^{-1}$ to 0.7 $nm^{-1}$ and is therefore only a qualitative measure of the changes of the scattering curve. As evidenced in Figure S45, the presence of BSA does not significantly influence the trend of Q and I (q=6.1 $nm^{-1}$).

In the presence or absence of BSA, the nuclei appears to have already formed within the first 100 ms. Then, Q slightly increases during the first 10 s of the reaction suggesting a predominant process related to the reorganization of the particles.[13] After 10 seconds, Q started to decrease and plateau after 100 s. This trend is related to the amorphous particles formed within the first 10 s crystallizing to larger structures in the remaining 100 s. This hypothesis is supported by the analysis of the evolution of the intensity of the (110) diffraction peak of the BioHOF-1 at 6.1 $nm^{-1}$ (Figure S46). In fact, within the first 50 s of measurements, no diffraction peaks were observed. Conversely, after 50 s, it was possible to clearly observe the (110) reflection of the BioHOF-1 and to monitor the increasing of its integrated area over time. In both cases, the integrated area of the (110) peak reached its maximum after around 200 seconds. The kinetic of formation of BioHOF-1 crystals was further investigated via optical microscopy: the solutions of the two ligands were mixed in a vial and then 5 µL of the mixture was immediately drop-casted on a microscope slide. Several images of the drop-casted mixture were collected at different growth times using a 20x objective (Figure S47). It is possible to identify the presence of a large number of small particles after 30 s. Micrometrics BioHOF-1 crystals with needle-like morphology could be observed after 60 s. The number of these needle-like crystals rapidly increased in the first 120 s of the synthesis. Afterwards, the number of visible crystals slowly grew until the apparent completion of the synthesis after 300 seconds. These images further support the conclusion made from the analysis of the time-resolved SAXS data. With the employed set-up and in the investigated timeframe, the presence of BSA did not play a significant role in the kinetic of the particle growth. The mechanism of formation of BSA@BioHOF-1 composite material could be defined as an encapsulation process.

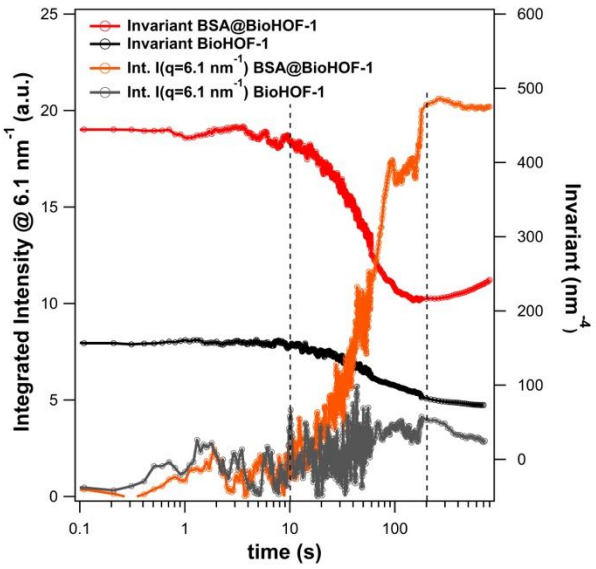


Figure S45. Integrated intensity of the (100) reflection of BioHOF-1 at 6.1 $nm^{-1}$ (I ($q$=6.1 $nm^{-1}$)) and Invariant Q calculated from Time-Resolved SAXS for the synthesis of BioHOF-1 and BSA@BioHOF-1.

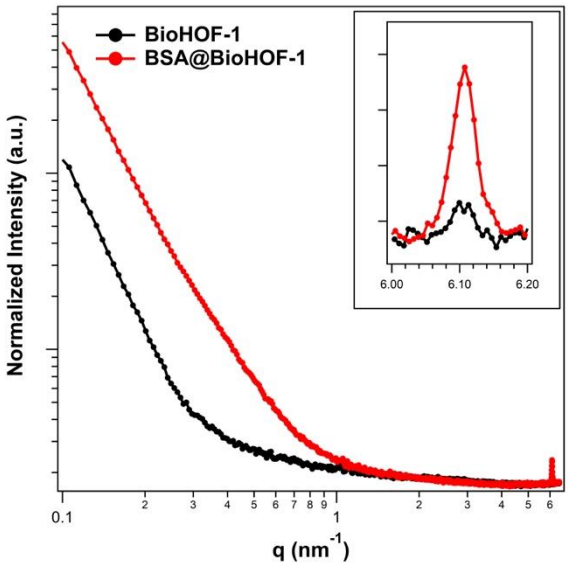


Figure S46. Normalized SAXS patterns of the BioHOF-1 (red) and BSA@BioHOF-1 (black) after 700 s of growth.

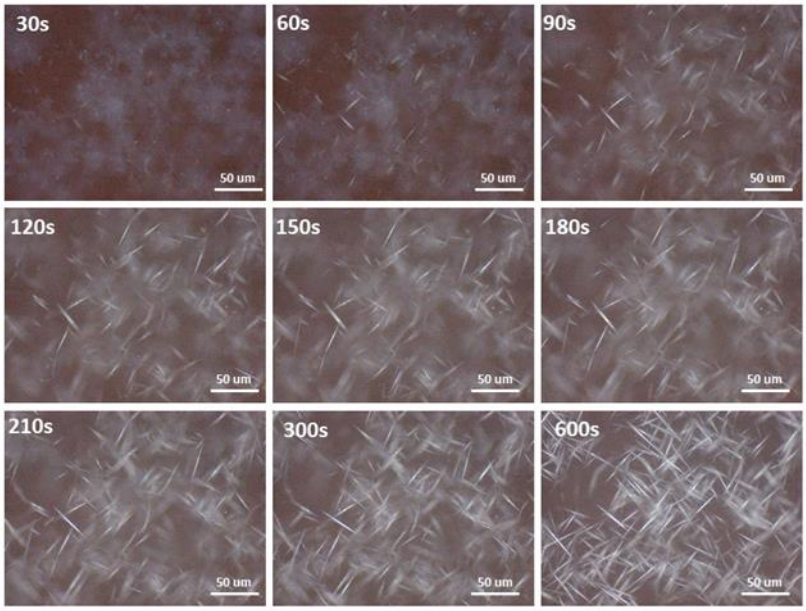


Figure S47. Optical microscope (20× objective) images collected during the synthesis of BioHOF-1 (Protocol 1, **1** (10 μL) + **2** (10 μL), mixed once with the micropipette and then immediately drop-cast on a microscope glass).

**Additional porosity**

To further investigate the hierarchical pore structure of the BSA@BioHOF-1 biocomposite, the SAXS patterns were analyzed after 700 s of growth. The SAXS patterns of both the BioHOF-1 and BSA@BioHOF-1 were fitted with a hierarchical model of large structures represented by the HOF crystals with non-correlated pores replicated by the BSA into the HOF crystals (Figure S48). Considering the large size of the HOF particles, the BSA@BioHOF-1 data fit showed the presence of two distinctive components: (i) a Power Law component related to the large particles (>300 nm) and (ii) a Guinier knee that is related to the presence of mesopores (Figure S48) This Guinier knee has been modeled by non interacting spherical pores following a Schulz distribution for their number size distribution.[14, 15] The Guinier Radius has been calculated from the mean value of the volume size distribution. The calculated values for the radius of gyration ($R_g$) of the mesopores is 4.9 ± 0.5 nm. The size of these mesopores is sufficient to accommodate isolated BSA molecules ($R_g$ = 3.02 nm )[16]. Conversely, pure HOF obey only to a Power law, which is related to the aggregation of the large HOF particles. Thus, mesopores are absent in pure HOF. This hierarchical pore structure is compatible with the one reported models of porous biocomposites encapsulating BSA.[17]

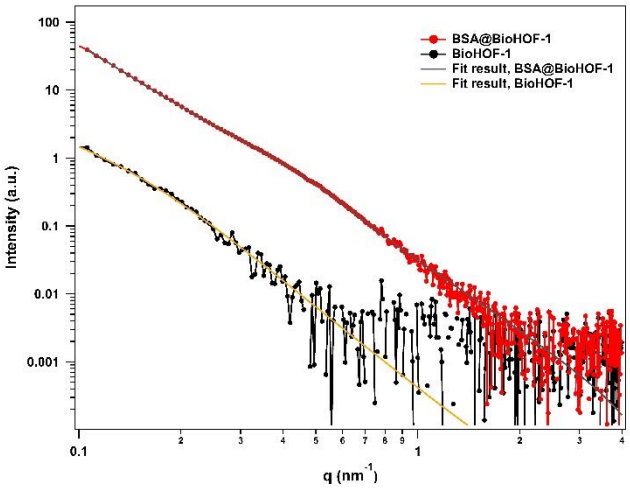


Figure S48. Background-subtracted SAXS patterns and fitted SAXS patterns of BioHOF-1 (red) and BSA@BioHOF-1 (black) after 700 s of growth.

## S11. References


1. Sheldon, R. A., *Cross-Linked Enzyme Aggregates as Industrial Biocatalysts*. *Org. Process Res. Dev.* **2011,** 15, 213-223.
2. Tükel, S. S.; Hürrem, F.; Yildirim, D.; Alptekin, Ö., *Preparation of crosslinked enzyme aggregates (CLEA) of catalase and its characterization*. *J. Mol. Catal. B: Enzym.* **2013,** 97, 252-257.
3. Boer, S., Morshedi, M., Tarzia, A, Doonan, C. J. , White, N. G., *Molecular Tectonics: node-and-linker building block approach to a family of hydrogen bonded frameworks*. *Chem. Eur. J.* **2019,** 25, 10006-10012.
4. Velásquez-Hernández, M. d. J.; Ricco, R.; Carraro, F.; Limpoco, F. T.; Linares-Moreau, M.; Leitner, E.; Wiltsche, H.; Rattenberger, J.; Schröttner, H.; Frühwirt, P.; Stadler, E. M.; Gescheidt, G.; Amenitsch, H.; Doonan, C. J.; Falcaro, P., *Degradation of ZIF-8 in phosphate buffered saline media*. *CrystEngComm* **2019,** 21, 4538-4544.
5. Luzuriaga, M. A.; Benjamin, C. E.; Gaertner, M. W.; Lee, H.; Herbert, F. C.; Mallick, S.; Gassensmith, J. J., *ZIF-8 degrades in cell media, serum, and some—but not all—common laboratory buffers*. *Supramol. Chem.* **2019**, DOI: 10.1080/10610278.2019.1616089.
6. Socrates, G., *Infrared and Raman Characteristic Group Frequencies: Tables and Charts, 3rd Edition*. Wiley: 2004.
7. Kumari, G.; Jayaramulu, K.; Maji, T. K.; Narayana, C., *Temperature Induced Structural Transformations and Gas Adsorption in the Zeolitic Imidazolate Framework ZIF-8: A Raman Study*. *J. Phys. Chem. A* **2013,** 117, 11006-11012.
8. Ethiraj, J.; Bonino, F.; Lamberti, C.; Bordiga, S., *H2S interaction with HKUST-1 and ZIF-8 MOFs: A multitechnique study*. *Micropor. Mesopor. Mat.* **2015,** 207, 90-94.
9. Ozimek, P.; Veenhuis, M.; van der Klei, I. J., *Alcohol oxidase: A complex peroxisomal, oligomeric flavoprotein*. *FEMS Yeast Res.* **2005,** 5, 975-983.
10. Grillo, I., *Applications of stopped-flow in SAXS and SANS*. *Curr. Opin. Colloid Interface Sci.* **2009,** 14, 402-408.
11. Amenitsch, H.; Rappolt, M.; Kriechbaum, M.; Mio, H.; Laggner, P.; Bernstorff, S., *First performance assessment of the small-angle X-ray scattering beamline at ELETTRA*. *J. Synchrotron Rad.* **1998,** 5, 506-508.
12. O. Glatter, O. K., *Small Angle X-ray Scattering*. Academic Press Inc.: London, 1982.
13. Bolze, J.; Pontoni, D.; Ballauff, M.; Narayanan, T.; Cölfen, H., *Time-resolved SAXS study of the effect of a double hydrophilic block-copolymer on the formation of CaCO3 from a supersaturated salt solution*. *J. Colloid Interface Sci.* **2004,** 277, 84-94.
14. Kotlarchyk, M.; Chen, S. H., *Analysis of small angle neutron scattering spectra from polydisperse interacting colloids*. *J. Chem. Phys.* **1983,** 79, 2461-2469.
15. Aragón, S. R.; Pecora, R., *Theory of dynamic light scattering from polydisperse systems*. *J. Chem. Phys.* **1976,** 64, 2395-2404.
16. Pernot, P.; Round, A.; Barrett, R.; De Maria Antolinos, A.; Gobbo, A.; Gordon, E.; Huet, J.; Kieffer, J.; Lentini, M.; Mattenet, M.; Morawe, C.; Mueller-Dieckmann, C.; Ohlsson, S.; Schmid, W.; Surr, J.; Theveneau, P.; Zerrad, L.; McSweeney, S., *Upgraded ESRF BM29 beamline for SAXS on macromolecules in solution*. *J. Synchrotron Rad.* **2013,** 20, 660-664.
17. Liang, K.; Ricco, R.; Doherty, C. M.; Styles, M. J.; Bell, S.; Kirby, N.; Mudie, S.; Haylock, D.; Hill, A. J.; Doonan, C. J.; Falcaro, P., *Biomimetic mineralization of metal-organic frameworks as protective coatings for biomacromolecules*. *Nat. Commun.* **2015,** 6, 7240.